Title

Structural and molecular basis for Cardiovirus 2A protein as a viral gene expression switch

Author list

Chris H. Hill*†[1,2,3], Lukas Pekarek†[4], Sawsan Napthine†[1], Anuja Kibe[4], Andrew E. Firth[1], Stephen C. Graham*[1], Neva Caliskan*[4,5] and Ian Brierley*[1]

† These authors contributed equally

*corresponding authors:

Chris H. Hill: chris.hill@york.ac.uk
Stephen C. Graham: scg34@cam.ac.uk
Neva Caliskan: neva.caliskan@helmholtz-hiri.de
Ian Brierley: ib103@cam.ac.uk

Affiliations

[1] Division of Virology, Department of Pathology, University of Cambridge, Tennis Court Road, Cambridge, UK. CB2 1QP.

[2] MRC Laboratory of Molecular Biology, Cambridge Biomedical Campus, Francis Crick Ave, Cambridge, UK. CB2 0QH

[3] **Present address:** Department of Biology, University of York, Wentworth Way, York, YO10 5DD.

[4] Helmholtz Institute for RNA-based Infection Research (HIRI), Helmholtz Centre for Infection Research (HZI), Würzburg, Germany

[5] Medical Faculty, Julius-Maximilians University Würzburg, Josef-Schneider-Straße 2/D15, 97080 Würzburg, Germany

Abstract

Programmed –1 ribosomal frameshifting (PRF) in cardioviruses is activated by the 2A protein, a multi-functional virulence factor that also inhibits cap-dependent translational initiation. Here we present the X-ray crystal structure of 2A and show that it selectively binds to a pseudoknot-like conformation of the PRF stimulatory RNA element in the viral genome. Using optical tweezers, we demonstrate that 2A stabilises this RNA element, likely explaining the increase in PRF efficiency in the presence of 2A. Next, we demonstrate a strong interaction between 2A and the small ribosomal subunit and present a cryo-EM structure of 2A bound to initiated 70S ribosomes. Multiple copies of 2A bind to the 16S rRNA where they may compete for binding with initiation and elongation factors. Together, these results define the structural basis for RNA recognition by 2A, show how 2A-mediated stabilisation of an RNA pseudoknot

promotes PRF, and reveal how 2A accumulation may shut down translation during virus infection.

Introduction

PRF is a translational control strategy employed by many RNA viruses, where it ensures the production of proteins in optimal ratios for efficient virus assembly and enables viruses to expand their coding capacity through the utilisation of overlapping ORFs (reviewed in[1-3]). In canonical PRF, elongating ribosomes pause over a heptanucleotide "slippery sequence" of the form X_XXY_YYZ when they encounter a "stimulatory element" about 5–9 nucleotides downstream in the mRNA. During this time, a –1 frameshift may occur if codon-anticodon re-pairing takes place over the X_XXY_YYZ sequence: the homopolymeric stretches allow the tRNA in the P-site to slip from XXY to XXX, and the tRNA in the A-site to slip from YYZ to YYY[4-7]. A diverse array of stem-loops and pseudoknots are known to induce frameshifting, and the stability, plasticity and unfolding kinetics of these RNA elements are thought to be the primary determinants of PRF efficiency[8-10], along with the thermodynamic stability of the codon-anticodon interactions[6]. Cardioviruses present a highly unusual variation to conventional viral PRF in which the virally encoded 2A protein is required as an essential *trans*-activator[11,12]. Here, the spacing between the slippery sequence and stem-loop is 13 nt, significantly longer than typically seen, and 2A protein has been proposed to bridge this gap through interaction with the stem-loop[12]. This allows for temporal control of gene expression as the efficiency of –1 frameshifting is linked to 2A concentration, which increases with time throughout the infection cycle[12].

2A is a small, basic protein (~17 kDa; 143 amino acids; pI ~9.1) generated by 3C-mediated proteolytic cleavage at the N-terminus[13] and Stop-Go peptide release at the C-terminus[14]. Despite the identical name, it has no homology to any other picornavirus "2A" protein[15], nor any other protein of known structure. The PRF-stimulatory activity of 2A is related to its ability to bind to the RNA stimulatory element[12]. However, 2A also binds to 40S ribosomal subunits[16], inhibits apoptosis[17] and contributes to host cell shut-off by inhibiting cap-dependent translation. A C-terminal YxxxxLΦ motif has been proposed to bind to and sequester eIF4E in a manner analogous to eIF4E binding protein 1 (4E-BP1)[16], thereby interfering with eIF4F assembly[18]. However, the absence of structural data has precluded a definitive molecular characterisation of this multi-functional protein, and the mechanism by which it recognises RNA elements and stimulates frameshifting remains obscure.

Here we present the crystal structure of 2A from encephalomyocarditis virus (EMCV), revealing a novel RNA-binding fold that we term a “beta-shell”. We show that 2A binds directly to the frameshift-stimulatory element in the viral RNA with nanomolar affinity and equimolar stoichiometry, and we define the minimal RNA element required for binding. Through site-directed mutagenesis and the use of single-molecule optical tweezers, we study the dynamics of this RNA element, both alone and in the presence of 2A. By observing short-lived intermediate states in real-time, we demonstrate that the EMCV stimulatory element exists in at least two conformations and 2A binding stabilises one of these, an RNA pseudoknot, increasing the force required to unwind it. Finally, we report a direct interaction of 2A with both mammalian and bacterial ribosomes. High-resolution cryo-electron microscopy (cryo-EM) characterisation of 2A in complex with initiated 70S ribosomes reveals a multivalent binding mechanism and defines the molecular basis for RNA recognition by the 2A protein. It also reveals a likely mechanism of 2A-associated translational modulation, by competing for ribosome binding with initiation factors and elongation factors. Together, our work provides a new structural framework for understanding protein-mediated frameshifting and 2A-mediated regulation of gene expression.

Results

Structure of EMCV 2A reveals an RNA-binding fold

Following recombinant expression in *E. coli*, purified 2A was analysed by SEC-MALS, revealing a predominantly monodisperse, monomeric sample (**Fig. 1a, b**; observed mass 18032.8 Da vs calculated mass 17930.34 Da), with a small proportion of dimers (observed mass 40836.0 Da). We crystallised the protein and determined the structure by multiple-wavelength anomalous dispersion analysis of a selenomethionyl derivative. The asymmetric unit (ASU) of the $P6_222$ cell contains four copies of 2A related by non-crystallographic symmetry (NCS), and the structure was refined to 2.6 Å resolution (**Supplementary Table 1**). Unexpectedly, the four molecules are arranged as a pair of covalent ‘dimers’ with an intermolecular disulfide bond forming between surface-exposed cysteine residues (C111). This arrangement is likely an artefact of crystallisation, which took >30 days, possibly due to the gradual oxidation of C111 promoting formation of the crystalline lattice. The N-terminal 10–12 residues are disordered in all chains except B, in which they make long-range contacts with another chain. Similarly, C-terminal residues beyond 137 are absent or poorly ordered in all chains.

2A adopts a compact, globular fold of the form $\beta_3\alpha\beta_3\alpha\beta$ (**Fig. 1c**). Searches of PDBeFOLD[19], DALI[20] and CATHEDRAL[21] databases failed to reveal structural homology to any other protein, so we term this fold a "beta shell". The most striking feature is a curved, seven-stranded anti-parallel beta sheet (**Fig. 1d**). The concave face of the beta sheet is supported by tight packing against the two alpha helices: together, this comprises the hydrophobic core of the fold. In contrast, the solvent-exposed convex face and surrounding loops are enriched with arginine, lysine and histidine residues, conferring a strong positive electrostatic surface potential at physiological pH. Superposition of the four NCS-related chains and an analysis of the atomic displacement factors reveals regions of flexibility (**Fig. 1e, f**). In addition to the N- and C-termini, the β2-loop-β3 region (residues 28–37) exists in multiple conformations that deviate by up to 5.8 Å in the position of the C_α backbone. Similarly, the arginine-rich loop between β5 and β6 ("arginine loop", residues 93–100) is mobile, with backbone deviations of up to 4.5 Å.

Several previous studies have described mutations, truncations or deletions in EMCV 2A that affect its activity[22-24]. Many of the truncations would severely disrupt the fold and the results obtained with these mutants should be interpreted with caution. However, the loop truncation ($2A_{\Delta 94\text{-}100}$) and point mutations made by Groppo *et al.*[23] would have only minor effects (**Supplementary Fig. 1**). Notably, in 2A, a C-terminal YxxxxLΦ motif predicted to bind eIF4E is within a beta strand, whereas the equivalent motif in 4E-BP1 is alpha-helical[25]. As a result, Y129 is partially buried and distal to both L134 and I135. Overlay of our 2A structure with the structure of the eIF4E:4E-BP1 complex indicates that without a significant conformational change, this motif is unlikely to represent the mechanism by which 2A recognises eIF4E (**Supplementary Fig. 1**).

2A binds to a minimal 47 nt pseudoknot in the viral RNA

The RNA sequence that directs PRF in EMCV consists of a G_GUU_UUU slippery sequence and a stimulatory stem-loop element downstream (**Fig. 2a**). We have previously demonstrated that three conserved cytosines in the loop are essential for 2A binding[12] (**Fig. 2a**). To map the interaction between 2A and the stimulatory element in more detail, we prepared a series of synthetic RNAs with truncations in the shift site, loop, and 5′ and 3′ extensions on either side of the stem (EMCV 1–6; **Fig. 2b**). These were fluorescently labelled at the 5′ end, and their binding to 2A was analysed by electrophoretic mobility shift assay (EMSA; **Fig. 2c**) and microscale thermophoresis (MST; **Fig. 2d, Supplementary Table 2**).

Binding of 2A to EMCV 1 RNA is high affinity (K_D = 360 ± 34 nM). Removal of the 3′ extension, as in EMCV 3 and EMCV 6, further increases the affinity (K_D values of 40 ± 2 and 70 ± 14 nM, respectively), perhaps by removing competing base-pairing interactions. There is no substantial difference between affinities of EMCV 3 and 6, which differ only by the presence of the shift site. Removal of the 5′ extension, as in EMCV 2 and EMCV 4, completely abolishes 2A binding, and truncation of the loop, including a putative second stem (EMCV 5) reduces binding to micromolar levels. Truncating the disordered N- and C- termini of 2A, or mutating the disulfide-forming C111 residue has no effect on RNA binding (**Supplementary Fig. 2**). To investigate stoichiometry, we performed an isothermal titration calorimetry (ITC) analysis of the interaction between 2A and EMCV 6 (**Supplementary Fig. 2**). Equimolar binding was observed, with a measured K_D (246 ± 72 nM), similar to those obtained using MST. The dominance of enthalpy (ΔH, –13.9 ± 0.81 kcal/mol) to the overall free energy of binding (ΔG, –9.02 kcal/mol) indicates an interaction mechanism driven by hydrogen bond or electrostatic contact formation. Finally, reciprocal MST experiments with fluorescently labelled 2A and unlabelled RNA yielded similar K_D values (**Supplementary Fig. 2**, **Supplementary Table 2**).

We next asked whether these small RNAs could act as competitors to sequester 2A and reduce the efficiency of PRF in rabbit reticulocyte lysate (RRL) *in vitro* translation reactions programmed with a frameshift reporter mRNA (**Supplementary Fig. 2**). Indeed, when unlabelled EMCV 1, 3 and 6 were added in excess, they were able to compete with the stimulatory element present in the reporter, thereby reducing the amount of the –1 frame product. In contrast, EMCV 2, 4 and 5 had no such effect, reinforcing the results of direct binding experiments.

The failure of 2A to bind to EMCV 2, 4 and 5 was unexpected as these RNAs retain the main stem and the conserved cytosine triplet in the putative loop region. A possible explanation is that the frameshift-relevant state may include an interaction between the loop and the 5′ extension, forming a different conformation that 2A selectively recognises. To test this, we carried out mutagenesis of the 5′ extension and loop C-triplet. Individually, G7C and C37G mutations both reduce 2A-dependent PRF to near-background levels (**Supplementary Fig. 3**). However, in combination, the G7C+C37G double mutation restores PRF to wild-type levels, and EMSA experiments with these mutants confirm that this is due to inhibition and restoration of 2A binding. Together, this demonstrates the likelihood of a base-pair between positions 7 and 37 that is necessary to form a conformation that 2A selectively recognises.

Using this base pair as a restraint, RNA structure prediction[26,27] reveals a pseudoknot-like fold (**Supplementary Fig. 3**).

Single-molecule measurements of stimulatory element unwinding reveal several conformations

Information is limited in ensemble measurements of RNA-protein interactions due to molecular averaging. To further explore the effects of 2A on unfolding and refolding of individual EMCV RNA molecules, we used optical tweezers (**Fig. 3a**). In force-ramp experiments, a single RNA molecule is gradually stretched and relaxed in several cycles at a constant pulling rate. The applied force allows the RNA molecule to transition between folded and unfolded states, and sudden changes in recorded force-distance trajectories indicate transitions between RNA conformations (**Fig. 3c, d**)[28-30]. By mathematically fitting each force-distance curve (**Methods**) we can obtain information on the physical properties of the RNA such as the change in the contour length (maximum possible extension), which indicates whether our data are physically consistent with predicted structures of the EMCV RNA. In addition to the pseudoknot (40 nt, discussed above), *mfold*[31] suggested two other possible conformations for the frameshift stimulatory element: a stem loop (35 nt) and an extended stem-loop with additional interactions between 5' and 3' flanking regions (49 nt) (**Fig. 3b, Supplementary Table 6**). Alongside the wild-type EMCV RNA sequence (WT), we also used a mutant with a substitution in the cytosine triplet (CUC) which is known be crucial for 2A binding and PRF[12] (**Fig. 3a**; lower).

We initially monitored the unfolding and refolding of WT and CUC RNAs in the absence of 2A. In WT RNA, the majority of force-distance (FD) trajectories were characterized by a single rip at 9.3 ± 2.3 pN force (**Fig. 3c, e**). Upon release of the force, the molecules readily refolded at 6.5 ± 3.0 pN, showing that the process is reversible (**Fig. 3c, f, Supplementary Table 3**). The change in contour length calculated from the fits was approximately 26.3 ± 5.4 nm (**Supplementary Fig. 4, Supplementary Table 3**) corresponding to a length of 46 single-stranded nucleotides. This is in close agreement with the predicted 49 nt long extended stem-loop formed by the EMCV PRF RNA (**Fig. 3b, Supplementary Table 6**). Interestingly, we observed similar (un)folding trajectories with the CUC RNA, with a rip occurring at 8.6 ± 4.2 pN and a contour length change of about 27.2 ± 4.3 nm (**Fig. 3e, f, Supplementary Fig. 4, Supplementary Table 3**), suggesting both RNAs would essentially fold into a stem-loop of similar length.

In a small fraction of WT FD trajectories (~12 %) we observed a single unfolding event at higher forces above 20 pN, while refolding was unchanged (6.5 ± 3.0 pN), suggesting the existence of a WT conformer with resistance to unfolding. Indeed, the putative EMCV pseudoknot would comprise 40 nucleotides, and lead to an expected difference of 23 nm in contour length upon unfolding (**Supplementary Fig. 4, Supplementary Table 6**). Since both the predicted pseudoknot and extended-stem loop are of similar length, and the distributions of contour length change are quite broad, this parameter is not precise enough to unambiguously distinguish between these conformations. On the other hand, the resistance to unfolding and hysteresis during refolding are well-known characteristics of more complex structures such as pseudoknots[9,32], and this is also consistent with our mutational analysis (**Supplementary Fig. 3;** discussed above). Furthermore, these higher force unfolding events are not observed in the CUC mutant, which is very unlikely to form a pseudoknot (**Supplementary Fig. 4, Supplementary Table 3**).

Next, we compared the energetics of folding and unfolding of the conformers. In optical tweezer experiments, the work of unfolding is the work required to extend the folded RNA construct (dsDNA:RNA handles and dsRNA) minus the work required to extend the fully unfolded (dsDNA:RNA handles and ssRNA) construct ($W=W_{ds}-W_{ds+ss}$). Accordingly, free energy values of WT and CUC constructs were calculated as −13.6 ± 4.6 and −14.5 ± 4.7 kcal/mol, respectively, which are close to the *mfold*-predicted Gibbs free energy values for the stem loop (−14 ± 0.7 kcal/mol) and extended stem-loop (−16.2 ± 0.8 kcal/mol) (**Supplementary Table 3**). This further supports the view that the EMCV WT and CUC mutant RNAs predominantly fold into the predicted stem-loops.

2A favours the formation of an alternative conformation with resistance to mechanical unwinding

We next tested how 2A binding influences RNA stability and resistance of RNA to mechanical unwinding. For the wild-type RNA, global analysis of the unfolding forces reveals a 2A-induced stabilisation, which increased the fraction of unfolding events at higher forces (27.0 ± 4.2 pN) (**Fig. 3d, e, Supplementary Fig. 4, Supplementary Table 3**). However, refolding of the RNA was mostly unaffected (**Fig. 3d, f, Supplementary Table 3**). Probability distributions of the change in contour length show a peak at around 20.0 ± 3.4 nm (**Supplementary Fig. 4, Supplementary Table 3**) which may reflect the unfolding of either the stem-loop (21 nm

expected) or the proposed pseudoknot conformation (23 nm expected) (**Fig. 3b, Supplementary Fig. 4**, **Supplementary Table 6**).

Subsequently, we examined 2A binding to the CUC mutant RNA (**Supplementary Fig. 4**). In contrast to the wild type RNA, within this population we did not observe any stabilisation in the presence of 2A (**Fig. 3e, Supplementary Fig. 4**). Thus, the unfolding and refolding force distributions overlap with those observed for CUC RNA in absence of 2A (**Fig. 3e**, **f**, **Supplementary Fig. 4**, **Supplementary Table 3**). We observed a small shift in the distribution of contour length changes towards lower values, which could be either due to non-specific interactions or stochastic noise. Overall, the lack of effect of 2A on the CUC RNA agreed well with the ensemble analysis of 2A:RNA interactions.

To further dissect the effect of 2A on EMCV RNAs, we calculated the work performed on the WT and CUC RNAs during (un)folding in the presence of 2A (**Supplementary Fig. 4**). For CUC RNA with 2A, the unfolding and refolding work distributions were largely overlapping, so the process can be considered reversible. We obtained a free energy value of –15.5 ± 5.0 kcal/mol, which is within the range of *mfold* predicted free energy values for the CUC stem-loop (–14 ± 0.7 kcal/mol) and the extended stem-loop (–16.2 ± 0.8 kcal/mol). For WT RNA with 2A, the stabilisation effect shifted the calculated free energy to –26.5 ± 8.7 kcal/mol, thus moving the system away from equilibrium (**Supplementary Table 3**)[33,34]. The 2A-induced decrease in free energy of the wild-type RNA may be a combination of stabilisation induced by protein binding, and a change in RNA conformation. Taken together, our results support that 2A binding stabilises the EMCV stimulatory RNA element and increases its resistance to mechanical unwinding.

2A interacts with the small ribosomal subunit in both eukaryotes and prokaryotes

In addition to its role as a component of the stimulatory element, 2A has been reported to bind to 40S subunits in EMCV-infected cells[16]. To determine if the interaction of 2A with the 40S subunit can be reproduced *ex vivo*, we purified ribosomal subunits from native RRL and analysed 2A-subunit interactions by MST (**Fig. 4a, b**). Consistent with previous data, 2A forms a tight complex with 40S (apparent K_D = 10 ± 2 nM) but not 60S. This apparent selectivity for the small subunit was also observed with purified prokaryotic ribosome subunits. 2A binds with very high affinity to 30S (apparent K_D = 4 ± 1 nM; **Fig. 4c**), but not 50S (**Fig. 4d**). We next

examined binding of 2A to intact 70S ribosomes and to reconstituted, mRNA-bound 70S ribosomes at the initiation stage (70S IC; initiator $tRNA^{Met}$ in the P-site and an empty A-site). We were able to detect high affinity interactions with both uninitiated and initiated 70S ribosomes (**Fig. 4e, f**).

Prokaryotic ribosomes are responsive to 2A-mediated frameshifting

Prokaryotic translation systems are well-established models for studying eukaryotic PRF signals[35,36] but it is unknown whether they can support protein-dependent PRF. To address this, we measured the efficiency of the EMCV signal in a reconstituted prokaryotic translation system and in *E. coli* S30 extracts using frameshift reporter mRNAs (**Supplementary Fig. 5**). In each case, 2A-dependent PRF was observed, with ~7% of ribosomes changing frame. Mutagenesis of either the shift site or the CCC triplet disabled PRF. Shortening the length of the spacer to one more optimal for prokaryotic ribosomes (from 13 to 12 nt) doubled PRF efficiency to ~15%, comparable to that measured in eukaryotic *in vitro* translation systems (20%)[12]. High concentrations of 2A also had an inhibitory effect on translation, similar to that seen in eukaryotic systems.

Cryo-EM structure of a 2A-ribosome complex reveals the structural basis for RNA recognition and translational pathology

Having validated the use of prokaryotic ribosomes as a model system to study protein-dependent PRF, we prepared complexes between 2A and the initiated 70S ribosomes and imaged them by cryo-EM (**Fig. 5a, Supplementary Table 4**). After processing (**Supplementary Fig. 6**), the final 3D reconstruction produced a density map of 2.7 Å resolution and revealed three copies of 2A bound directly to 16S rRNA of the 30S subunit in a tripartite cluster (**Fig. 5b, c**). The local resolution for 2A was sufficient to allow sidechain modelling and refinement. All three 2A molecules use the same RNA-binding surface (comprising variations of R46, K48, K50, K73, K94, R95 and R97) (**Fig. 5d**), to recognise the ribose phosphate backbone through numerous polar and electrostatic contacts (**Fig. 6a–c**). We mutated this putative interaction surface (**Supplementary Fig. 5**) and observed reduced binding to both the stimulatory element RNA and mammalian ribosome subunits and a decreased activity in stimulating PRF *in vitro*. $2A_{R95A/R97A}$ was completely functionally defective, whilst $2A_{K73A}$ and $2A_{R46A/K48A/K50A}$ exhibited moderate and mild effects, respectively.

By comparing the quality of both the overall density for each 2A molecule, and the side-chain density at the interaction surface, we can rank the three binding sites 2A1 > 2A2 > 2A3 in order of likely affinity. 2A1 is the most well-ordered molecule, and the 2A1 binding site on the rRNA is also the most conserved between prokaryotic and mammalian ribosomes (**Supplementary Fig. 7**) This is therefore likely the most physiologically relevant site, and it is possible that 2A2 and 2A3 represent lower-affinity sites (a ~40-fold molar excess of 2A was used to prepare grids). 2A1 exemplifies the critical role of the "arginine loop" (**Fig. 6d**). R95, R97 and R100 side chains are inserted into a ~90° junction between helices 3 and 4, forming a network of electrostatic interactions that bridge the phosphate groups on both strands. This is further stabilised by the guanidinium groups stacking against each other and exposed bases (G38) (**Fig. 6d**). Arginine loop residues also form polar and electrostatic contacts at the 2A2 and 2A3 interfaces (**Fig. 6e, f**). Whilst base-specific contacts are rare, 2A2 interacts with U485 which is normally flipped out of helix 17 (**Supplementary Fig. 8**). Superposition of the rRNA binding sites failed to reveal a common structural motif for RNA recognition (**Supplementary Fig. 7**), thus conformational plasticity of side chains at the RNA-binding surface (**Fig. 5d**) explains how this protein can recognise a several RNA targets. There are also intermolecular contacts between 2A protomers, consistent with our observations of multimers by SEC-MALS (**Fig. 1b**) and EMSA (**Fig. 2c**). In a subset of the data, a fourth copy of 2A (2A4) was identified to bind helix 33 of the 16S rRNA 'beak' in the 30S head. Although local resolution was only sufficient for docking, 2A4 uses the same RNA-binding surface to recognise the distorted helical backbone (**Supplementary Fig. 8**).

The ribosome is in an unrotated state that would normally be elongation competent, with fMet-$tRNA_i$ base-paired to the initiator codon in the P-site and mRNA available for amino-acyl tRNA delivery to the A-site[37] (**Fig. 7a**). There are no 2A-induced rearrangements at the decoding centre (**Supplementary Fig. 8**) but the presence of 2A on the 30S subunit occludes the binding site for translational GTPases. 2A1 occupies a position that would severely clash with domain II of EF-G in both compact and extended pre- and post-translocation states[38,39] (**Fig. 7b**). It also makes direct hydrophobic contacts with the face of S12 that would normally interact with domain III of EF-G. This 2A interaction surface on S12 is directly adjacent to the binding site for antibiotic dityromycin, which inhibits translocation by steric incompatibility with the elongated form of EF-G[40] (**Supplementary Fig. 8**). 2A1 would also clash significantly with domain II of EF-Tu during delivery of aminoacyl tRNAs to the A-site[41,42] (**Fig. 7c**). In a similar way, 2A2 would be detrimental to both EF-G and EF-Tu binding (**Fig. 7b, c**). We therefore predict that 2A binding would be inhibitory to elongation and potentially initiation, via competition with IF2 during pre-initiation complex assembly[43].

Discussion

Here we show that 2A adopts an RNA-binding fold, allowing specific recognition and stabilisation of the PRF stimulatory element in the viral RNA and direct binding to host ribosomes. Given this structural framework, we can reinterpret several preceding biochemical and virological observations. Many functions of 2A can be assigned to a single positively charged surface loop ("arginine loop" residues 93–100). Despite the low pairwise sequence identity of 2A proteins amongst Cardioviruses, R95 and R97 are completely conserved. This region was originally described as a nuclear localisation sequence (NLS)[23] and subsequently, we demonstrated that these residues are essential for PRF activity in both EMCV and Theiler's murine encephalomyelitis virus (TMEV), and that their mutation to alanine prevents 2A binding to the stimulatory element in the viral RNA[12,44] (**Supplementary Fig. 5**). Here we reveal how R95 and R97 also mediate direct 2A binding to the small ribosomal subunit (**Fig. 6d–f**) and therefore also likely confer other 2A-associated translational activities. Importantly, 2A uses the same molecular surface to bind to both the PRF stimulatory element and to ribosomes (**Fig. 6d–f, Supplementary Fig. 5**), so for any given 2A molecule these events are mutually exclusive. This suggests that the primary determinant of –1 PRF is likely to be 2A binding to the stimulatory element, with ribosome binding having a secondary effect. If 2A were to act as a "bridge" between the stimulatory element and the ribosome, this would necessitate two separate interactions surfaces, which we do not observe.

Our cryo-EM structure unexpectedly revealed four distinct 2A:rRNA interfaces (**Fig. 6 and Supplementary Fig. 8**). Based on the quality of cryo-EM density and the degree of structural conservation between prokaryotic and mammalian ribosomes, the 2A1 site is likely to be the highest affinity and most physiologically relevant (**Supplementary Fig. 7**). Nevertheless, all sites provide clues as to how RNA-binding specificity is achieved. RNA recognition is driven almost exclusively by electrostatic interactions between arginine or lysine side chains and the ribose phosphate backbone oxygen atoms. The mobility and flexibility of the arginine loop and other residues at the RNA binding surface (**Fig. 1f, 5d**) illustrates how 2A can recognise a variety of structurally degenerate targets. Whilst superposition of sites failed to reveal a common structural motif (**Supplementary Fig. 7**), they all include features such as kinks, distortions and junctions between multiple helices. A preference for these features is consistent with our biochemical observations that 2A is unable to bind EMCV 2, 4 and 5 RNAs, which are predicted to form stable, undistorted stem-loops (**Fig. 2c, d**). There is a strong likelihood that, in the 2A-bound state, the conformation of the EMCV RNA that stimulates PRF

involves additional base-pairs between C-residues in the loop and a GG pair in the 5′ extension (**Supplementary Fig. 3**). This pseudoknot-like conformation may either pre-exist in equilibrium with other states, or it may be directly induced by 2A binding (**Fig. 8**). Whilst we have been unable to capture a snapshot of this molecular recognition event, it likely comprises the structural basis for the molecular "switch" that activates frameshifting during EMCV infection.

Our single-molecule data now also provide a physical explanation for this molecular "switch". It was previously shown that ribosome can exert forces of up to 20 pN during elongation[45]. We show that, in the absence of 2A, both WT and CUC RNAs unfold at forces around ~10 pN, well within the ribosome-achievable force range and hence unlikely to cause a ribosomal pause. However, in the presence of 2A, WT but not CUC RNAs are stabilised to unwind at ~27 pN, presenting a considerable blockade to ribosome progression (**Fig. 3d**). This also supports the idea that the failure of the CUC mutant to stimulate PRF is due to its inability to adopt the pseudoknot-like conformation of the "switch" that would normally be selectively recognised and stabilised by 2A.

Our current mechanistic understanding of PRF is largely informed by ensemble kinetic and single-molecule FRET studies of prokaryotic ribosomes[4-6,46-48]. Frameshifting occurs late during the EF-G mediated translocation step, in which the stimulatory element traps ribosomes in a rotated or hyper-rotated state, accompanied by multiple abortive EF-G binding attempts and rounds of GTP hydrolysis. Stability of the RNA stimulatory element structure downstream of the slippery sequence is thought to be an important determinant of the frameshifting efficiency[9,49,50] although the plasticity of this structure, and the ability to adopt alternate conformations, is also a key property[10]. Several recent studies emphasise the importance of the energetics of codon:anticodon base-pairing at the slippery sequence[6,51], suggesting that the primary role of the stimulatory element is to simply pause the ribosome over a permissive slippery sequence in which the tRNA-mRNA base pairing energies in the 0 and –1 frames are similar. Longer pauses at a more stable stimulatory element allow an equilibrium to be established between the 0 and –1 frames, converging on a maximum frameshift efficiency of ~50%. We have demonstrated how 2A-mediated stabilisation of the stimulatory element likely presents a potent elongation blockade allowing this equilibrium to be established (**Fig. 3e, 8**). However, this mechanism alone cannot explain the very high PRF efficiencies (up to ~70%) observed by ribosome profiling during EMCV infection[12,44].

Based on our structure, it is tempting to speculate that competition between EF-G/eEF2 and 2A1 binding might have a role in prolonging the pause, thereby contributing to the high PRF efficiencies that we observe in 2A-dependent systems[52]. Indeed, direct interactions between the ribosome and PRF stimulatory elements are not unprecedented, with a recent study describing how the HIV-1 stem-loop induces a pause by binding to the 70S A-site and preventing tRNA delivery[48]. The ribosome-bound form of 2A that we observe could therefore be a secondary 'enhancer' of PRF efficiency, acting synergistically with the main stimulatory element. It could also be relevant to the resolution of the elongation blockade: by providing an alternative 2A-binding surface that competes with the viral RNA, the ribosome may help to induce 2A dissociation from the stimulatory element during a pause at the PRF site. Alternatively, it may not be directly relevant to frameshifting *per se*, instead representing a way of interfering with host cell translation as 2A accumulates during infection.

In conclusion, this work defines the structural and molecular basis for the temporally regulated 'switch' behind the reprogramming of viral gene expression in EMCV infection (**Fig. 8**). At the heart of this is 2A: an RNA-binding protein with the remarkable ability to discriminate between stem-loop and pseudoknot conformers of the PRF stimulatory element. We also reveal how 2A interferes with host translation by specifically recognising distinct conformations within the ribosomal RNA. Together, this illustrates how the conformational plasticity of one RNA-binding surface can contribute to multiple functions through finely tuned relative affinities for different cellular targets.

Methods

Materials availability

Further information and requests for resources should be directed to and will be fulfilled by Ian Brierley (ib103@cam.ac.uk). Plasmids generated in this study are available on request. DNA and RNA oligonucleotides are standard synthetic products that are commercially available (see **Supplementary Table 5**).

Cloning, protein expression and purification

All gene cloning, manipulation and plasmid propagation steps involving pGEX6P1 or pOPT vectors were carried out in *Escherichia coli* DH5α cells grown at 37 °C in 2 × TY or LB media supplemented with appropriate selection antibiotics. EMCV 2A cDNA was amplified by PCR

from previously described plasmid 2A_pGEX6P1[12] (primers E2A_F1 and E2A_R1; **Supplementary Table 5**) and cloned into pOPTnH[53] using NdeI and BamHI sites, thereby introducing a C-terminal GlySerLysHis$_6$ tag. The 2A$_{9\text{-}136}$ truncated construct was cloned in an identical way (primers E2A_F2 and E2A_R2; **Supplementary Table 5**). The EMCV 2A R95A/R97A mutant was cloned into pOPTnH after PCR-amplification from a previously described 2A_pGEX6P1 construct containing these mutations[12]. Other EMCV 2A mutants were prepared by PCR mutagenesis, using either the wild-type EMCV 2A_pOPT or 2A$_{9\text{-}136}$_pOPT plasmids as templates, with the following primer pairs (C111S: E2A_mut_F1 and E2A_mut_R1; R46A/K48A/K50A: E2A_mut_F2 and E2A_mut_R2; K74A: E2A_mut_F3 and E2A_mut_R3; **Supplementary Table 5**). To introduce an N-terminal StrepII-tag ($_{SII\text{-}}$2A), annealed oligonucleotides encoding the StrepII-tag (SII_F and SII_R, **Supplementary Table 5**) were inserted in-frame at the BamHI site of 2A_pGEX6P1.

Recombinant proteins 2A, 2A$_{9\text{-}136;\ C111S,}$ 2A$_{R95A/R97A}$, 2A$_{R46A/K48A/K50A}$ and 2A$_{K73A}$ were expressed in *E. coli* BL21 (DE3) pLysS cells grown in 2 × TY broth supplemented with 100 µg/mL ampicillin and 12.5 µg/mL chloramphenicol (37 °C, 200 rpm) until an OD$_{600nm}$ of 0.6 – 1.0 was reached. Expression was induced with 0.5 mM IPTG for either 4 h at 37 °C or overnight at 21 °C. For selenomethionyl derivatisation (2A$_{SeMet}$), protein was expressed in *E. coli* B834 cells, grown shaking (210 rpm, 37°C) in SeMet base media (Molecular Dimensions) supplemented with nutrient mix, 40 µg/mL L-selenomethionine and 100 µg/mL ampicillin. Expression was induced as above.

Cells were harvested by centrifugation (4,000 × g, 4°C, 20 min), washed once in ice-cold PBS and stored at -20°C. Pellets from four litres of culture were resuspended in cold lysis buffer (50 mM Tris-HCl pH 8.0, 500 mM NaCl, 30 mM imidazole, supplemented with 50 µg/mL DNase I and EDTA-free protease inhibitors) and lysed by passage through a cell disruptor at 24 kPSI (Constant Systems). Lysate was cleared by centrifugation (39,000 × g, 40 min, 4°C) prior to incubation (1 h, 4°C) with 4.0 mL of Ni-NTA agarose (Qiagen) pre-equilibrated in the same buffer. Beads were washed in batch four times with 200 mL buffer (as above, but without DNase or protease inhibitors) by centrifugation (600 × g, 10 min, 4°C) and re-suspension. Washed beads were pooled to a gravity column prior to elution over 10 column volumes (CV) with 50 mM Tris-HCl pH 8.0, 150 mM NaCl, 300 mM imidazole. Fractions containing 2A were pooled and dialysed (3K molecular weight cut-off (MWCO), 4°C, 16 h) against 1 L buffer A (50 mM Tris-HCl pH 8.0, 400 mM NaCl, 5.0 mM DTT) before heparin-affinity chromatography to remove contaminating nucleic acids. Samples were loaded on a 10 mL HiTrap Heparin column

(GE Healthcare) at 2.0 mL/min, washed with two CV of buffer A and eluted with a 40% → 100% gradient of buffer B (50 mM Tris-HCl pH 8.0, 1.0 M NaCl, 5.0 mM DTT) over 10 CV. Fractions containing 2A were pooled and concentrated using an Amicon® Ultra centrifugal filter unit (10K MWCO, 4,000 × g). Size exclusion chromatography was performed using a Superdex 75 16/600 column pre-equilibrated in 10 mM HEPES pH 7.9, 1.0 M NaCl, 5.0 mM DTT. Purity was judged by 4-20% gradient SDS-PAGE, and protein identity verified by mass spectrometry. Purified protein was used immediately or was concentrated as above (~ 7.0 mg/mL, 390 µM), snap-frozen in liquid nitrogen and stored at -80°C. Variants of 2A, including $2A_{9\text{-}136;C111S}$ and $2A_{SeMet}$ were purified identically to the wild-type protein. The StrepII-tagged variant ($_{SII\text{-}}$2A) was expressed and purified using GST-affinity as previously described[12]. Following removal of the GST tag by 3C protease, $_{SII\text{-}}$2A was further purified by Heparin affinity and size-exclusion chromatography as above.

Size-exclusion chromatography coupled to multi-angle light scattering (SEC-MALS)

Per experiment, 100 µL of protein was injected onto a Superdex 75 increase 10/300 GL column (GE Healthcare) pre-equilibrated with 20 mM Tris-HCl, 1.0 M NaCl (0.4 mL/min flow, 25°C). Experiments were performed with 5.2 mg/mL 2A (corresponding to a molar concentration of 290 µM). The static light scattering, differential refractive index, and the UV absorbance at 280 nm were measured in-line by DAWN 8+ (Wyatt Technology), Optilab T-rEX (Wyatt Technology), and Agilent 1260 UV (Agilent Technologies) detectors. The corresponding molar mass from each elution peak was calculated using ASTRA 6.1 software (Wyatt Technology).

Protein crystallization

Purified EMCV 2A was concentrated to 5.9 mg/ml in 10 mM HEPES pH 7.9, 1.0 M NaCl, 2.0 mM DTT. Diffraction-quality native 2A crystals were grown at 21°C by sitting-drop vapor diffusion against an 80 µL reservoir of 0.625 M $(NH_4)_2SO_4$, 0.15 M tri-sodium citrate pH 5.7. Notably, crystal growth was only visible after 30 days. Drops were prepared by mixing 200 nL protein and 200 nL crystallization buffer. Selenomethionyl derivative 2A ($2A_{SeMet}$) was concentrated to 5.7 mg/mL in 10 mM HEPES pH 7.9, 1.0 M NaCl, 2.0 mM DTT, and diffraction-quality $2A_{SeMet}$ crystals were grown as above against an 80 µL reservoir of 0.675 M $(NH_4)_2SO_4$, 0.15 M tri-sodium citrate pH 5.7. Crystals were cryo-protected by the addition of 0.5 µL crystallization buffer supplemented with 20% v/v glycerol, prior to harvesting in nylon loops and flash-cooling by plunging into liquid nitrogen.

519

520 *X-ray data collection, structure determination, refinement and analysis*

521 Native datasets (**Supplementary Table 1**) of 900 images were recorded at Diamond Light
522 Source, beamline I03 (λ = 0.9796 Å) on a Pilatus 6M detector (Dectris), using 100%
523 transmission, an oscillation range of 0.2° and an exposure time of 0.04 s per image. Data were
524 collected at a temperature of 100 K. Data were processed with the XIA2[54] automated pipeline,
525 using XDS[55] for indexing and integration, and AIMLESS[56] for scaling and merging.
526 Crystallographic calculations were performed using the default software parameters unless
527 otherwise stated. Processing and refinement statistics are detailed in **Supplementary Table**
528 **1**. Resolution cut-off was decided by a $CC_{1/2}$ value ≥ 0.5 and an I/σ(I) ≥ 1.0 in the highest
529 resolution shell[57]. For multiple-wavelength anomalous dispersion (MAD) phasing experiments,
530 selenomethionyl derivative datasets were ecorded at beamline I03 (peak λ = 0.9796 Å,
531 12656.0 eV; hrem λ = 0.9763, 12699.4 eV; inflexion λ = 0.9797 Å, 12655.0 eV). Data were
532 processed as above using XIA2, XDS and AIMLESS. The structure was solved by three-
533 wavelength anomalous dispersion analysis of the selenium derivative (space group $P6_222$)
534 performed using the autoSHARP pipeline[58], implementing SHELXD[59] for substructure
535 determination, SHARP for heavy-atom refinement and phasing, SOLOMON[60] for density
536 modification and ARP/wARP[61] for automated model building. This was successful in placing
537 503/573 (87%) residues in the asymmetric unit, which comprised four copies of the protein
538 related by non-crystallographic symmetry (NCS). This initial model was then used to solve the
539 native dataset by molecular replacement with Phaser [62]. The model was completed manually
540 by iterative cycles of model-building using COOT 0.9.2 [63] and refinement with phenix.refine[64]
541 (Phenix build 1.18.1_3865), using local NCS restraints and one TLS group per chain. Upon
542 completion of model building, ISOLDE 1.1 (Croll, 2018) was used to improve model geometry
543 and resolve clashes prior to a final round of refinement using phenix.refine. MolProbity[65] was
544 used throughout the process to evaluate model geometry. For the electrostatic potential
545 calculations, partial charges were first assigned using PDB2PQR[66], implementing PROPKA
546 to estimate protein pKa values. Electrostatic surfaces were then calculated using APBS[67].
547 Prior to designation of the “beta shell” as a new fold, structure-based database searches for
548 proteins with similar folds to EMCV 2A were performed using PDBeFOLD[19], DALI[20] and
549 CATHEDRAL[21]. Buried surface areas were calculated using PDBePISA [68].

550

551 *RNA folding prediction*

552 The simRNAweb server[26] was used for stem-loop and pseudoknot tertiary structure modelling
553 of the EMCV stimulatory element. Experimentally-determined base-pairs were input as

secondary structure restraints. Replica exchange Monte Carlo (REMC) simulated-annealing was performed with 10 replicas and 16000000 iterations per cycle. Trajectory files from eight independent simulations were concatenated and clustered, and all-atom PDB files was generated from the lowest energy state in each of the five most populous clusters. The 3D models presented (**Supplementary Fig. 3**) represent the top cluster for pseudoknots and the top three clusters for stem-loops.

Electrophoretic Mobility Shift Assay (EMSA)

Synthetic RNA oligonucleotides (**Supplementary Table 5**, IDT) were dissolved in distilled water. RNAs were labelled at the 5′ end with A647-maleimide or Cy5-maleimide conjugates (GE Healthcare) using the 5′ EndTag kit (Vector Labs) as directed by the manufacturer. For each binding experiment, a series of reactions were prepared on ice, each containing 1.0 µL 500 nM RNA, 1.0 µL serially diluted protein at concentrations of 320, 160, 80, 40, 20, 10, 5.0, and 2.5 µM in 10 mM HEPES pH 7.9, 1.0 M NaCl, 5.0 µL 2 × buffer (20 mM Tris-HCl pH 7.4, 80 mM NaCl, 4.0 mM magnesium acetate 2.0 mM DTT, 10% v/v glycerol, 0.02% w/v bromophenol blue, 200 µg/mL porcine liver tRNA, 800 U /mL SUPERase-In [Invitrogen]) and 3.0 µL distilled water. This gave final binding reactions of 10 µL with 50 nM RNA, 1 × buffer, a salt concentration of ~ 140 mM and proteins at concentrations of 32, 16, 8.0, 4.0, 2.0, 1.0, 0.5 and 0.25 µM. Samples were incubated at 37°C for 20 min prior to analysis by native 10% acrylamide/TBE PAGE (25 min, 200 V constant). Gels were scanned with a Typhoon FLA-7000 (GE) using the 635 nm laser / R670 filter. Raw, uncropped image data is available in the **Source Data** file.

Isothermal Titration Calorimetry (ITC)

ITC experiments were performed at 25°C using an automated MicroCal PEAQ-ITC platform (Malvern Panalytical). Proteins and synthetic RNA oligonucleotides (IDT) were dialysed extensively (24 h, 4°C) into buffer (50 mM Tris-HCl pH 7.4, 400 mM NaCl) prior to experiments. RNA (52 µM) was titrated into protein (5 µM) with 1 x 0.4 µL injection followed by 12 × 3.0 µL injections. Control titrations of RNA into buffer, buffer into protein and buffer into buffer were also performed. Data were analysed using the MicroCal PEAQ-ITC analysis software 1.30 (Malvern Panalytical) and fitted using a one-site binding model. Presented traces were representative of two independent titrations.

Microscale Thermophoresis (MST)

For RNA-binding experiments, synthetic EMCV RNA variants (**Supplementary Table 5**) were dissolved in distilled water and labelled at the 5' end with Dylight 650 maleimide conjugates (Thermo Scientific) using the 5′ EndTag kit (Vector Labs) as directed by the manufacturer. For each binding experiment, RNA was diluted to 10 nM in MST buffer (50 mM Tris-HCl pH 7.8, 150 mM NaCl, 10 mM $MgCl_2$, 2 mM DTT supplemented with 0.05% Tween 20) and a series of 16 tubes with 2A dilutions were prepared on ice in MST buffer, producing 2A ligand concentrations ranging from 0.00015 to 5 µM for EMCV RNA 2-6 and 0.00006 to 20 µM for EMCV RNA1. For the measurement, each ligand dilution was mixed with one volume of labelled RNA, which led to a final concentration of 5.0 nM labelled RNA. The reaction was mixed by pipetting, incubated for 10 min followed by centrifugation at 10,000 × g for 10 min. Capillary forces were used to load the samples into Monolith NT.115 Premium Capillaries (NanoTemper Technologies). Measurements were performed using a Monolith NT.115Pico instrument (NanoTemper Technologies) at an ambient temperature of 25°C. Instrument parameters were adjusted to 5% LED power, medium MST power and MST on-time of 10 seconds. An initial fluorescence scan was performed across the capillaries to determine the sample quality and afterwards 16 subsequent thermophoresis measurements were performed. To determine binding affinities, data of at least two independently pipetted measurements were analysed for the fraction bound (MO.Affinity Analysis software, NanoTemper Technologies). For the non-binders, since the maximum amplitude would numerically be zero, deltaFnorm values were divided by the average maximum amplitude of the dataset to plot fraction bound. Data were fitted to the Kd model using MO.Affinity Analysis software (NanoTemper) and were plotted using Prism 8.0.2 (GraphPad).

Conjugation of a fluorescent label to the surface-exposed cysteine residue (C111) observed in the 2A crystal structure (**Fig. 1e**) provided a convenient way of studying binding to multiple unlabelled targets by MST, in such a way that the observed affinities would be directly comparable. For this experiment, EMCV 2A protein was labelled using the Protein Labelling Kit RED-Maleimide (NanoTemper Technologies) according to the manufacturer's instructions. In brief, 2A protein was diluted in a buffer containing 10 mM HEPES pH 7.9, 1.0 M NaCl and dye was mixed at a 1:3 molar ratio at room temperature for 30 min in the dark. Unreacted dye was removed on a spin gel filtration column equilibrated with 10 mM HEPES pH 7.9, 1.0 M NaCl. The labelled 2A protein was diluted to 10 nM in MST buffer. Synthetic EMCV RNA variants were used in dilutions ranging from 0.0008 to 26 µM for RNA 1 and 0.00003 to 1 µM for RNA 2-6. For the measurement, each RNA ligand dilution was mixed with one volume of labelled protein 2A, which led to a final concentration of protein 2A of 5.0 nM. Similar

experiments were conducted with ribosomes in MST buffer, with ligand concentrations ranging between 0.00002 to 0.4 µM for 40S and 60S, 0.00003 to 1 µM for 30S, 0.000027 to 0.9 µM for 50S, 0.0008 to 1.375 µM for empty 70S and 0.000003 to 0.1 µM for 70S IC. The measurements were performed as described above.

Preparation of constructs for optical tweezer experiments

DNA encoding the frameshifting sequence of EMCV was inserted into plasmid pMZ_lambda_OT using PCR and subsequent Gibson assembly. This plasmid contains the ColE1 origin, ampicillin resistance, ribosome binding site and two 2 kbp handle regions derived from lambda phage DNA (5′ and 3′ handle). For the generation of the mutant plasmid, PCR and blunt-end ligation was used to mutate the CCC triplet in the EMCV stem-loop to CUC. Control constructs (see below) were prepared the same way as mutant constructs. For the control construct without any single-stranded RNA region, a PCR reaction using the EMCV wild-type (CCC) construct as template was conducted with 3' handle forward oligonucleotide and 5' handle reverse oligonucleotide as primers (**Supplementary Table 5**) After the PCR, the linear products were blunt-end ligated to yield the control constructs. Wild-type and mutant plasmids were subsequently used to generate construct suitable for optical tweezer measurements consisting of the EMCV frameshifting sequence flanked by the 2 kbp long handle regions. Three pairs of primers for PCR were designed allowing the amplification of the *in vitro* transcription template and 5′ and 3′ handles. Subsequently, PCR reactions generated 5′ and 3′ handles and a long template for *in vitro* transcription. The 3′ handle was labelled during PCR using a 5′ digoxigenin-labelled reverse primer. The 5′ handle was labelled with Biotin-16-dUTP at the 3′ end following PCR using T4 DNA polymerase. RNA was transcribed from templates for *in vitro* transcription using T7 RNA polymerase. RNA and both DNA handles (5′ and 3′) were annealed together in a mass ratio 1:1:1 (5 µg each) by incubation at 95 °C for 10 min, 62 °C for 1 hour, 52 °C for 1 hour and slow cooling to 4 °C in a buffer containing 80% formamide, 400 mM NaCl, 40 mM HEPES, pH 7.5, and 1 mM EDTA[69]. Following annealing, the samples were concentrated by ethanol precipitation, the pellets resuspended in 40 µL RNase-free water, split into 4 µL aliquots and stored at –20 °C.

Optical tweezers data collection and analysis

Optical tweezer experiments were performed using a commercial dual-trap instrument equipped with a microfluidics system (C-trap, Lumicks). Optical tweezers (OT) constructs described above were mixed with 3 µL of polystyrene beads coated with antibodies against

digoxigenin (0.1% v/v suspension, Ø 1.76 µm, Lumicks), 8 µL of measurement buffer (20 mM HEPES, pH 7.6, 300 mM KCl, 5 mM $MgCl_2$, 5 mM DTT and 0.05% Tween) and 1 µL of RNase inhibitors. The mixture was incubated for 20 min at room temperature in a final volume of 16 µL, and subsequently diluted by addition of 0.5 mL measurement buffer. Separately, 0.8 µL of streptavidin-coated polystyrene beads (1% v/v suspension, Ø 2 µm, Lumicks) was supplemented with 1 mL of measurement buffer, the flow cell was washed with the measurement buffer and suspensions of both streptavidin beads as well as the complex of OT construct with anti-digoxigenin beads were introduced into the flow cell. Per experiment, an anti-digoxigenin (AD) bead and a streptavidin (SA) bead were optically trapped and brought into close proximity to allow the formation of a tether in between. The beads were moved apart (unfolding) and back together (refolding) at constant speed (0.05 µm/s) to yield the force-distance (FD) curves. The stiffness was maintained at 0.31 and 0.24 pN/nm for trap 1 (AD bead) and trap 2 (SA bead), respectively. For experiments with 2A protein experiments, protein was diluted to 300 nM in measurement buffer and added to the buffer channel of the optical tweezer flow cell. FD data was recorded at a rate of 78000 Hz. To ensure that the observed effects were indeed a result of interaction with the studied RNA region and not a non-specific binding to handle regions, we also employed constructs containing either no single-stranded RNA sequence (No ssRNA control) [http://dx.doi.org/10.17632/gkpwngy65h.2]. No oxygen scavengers were used during measurements. However, to prevent oxygen damage, all buffers were degassed and contained DTT as reducing agent.

Afterwards, the data were down sampled by a factor of 30 and filtered with a Butterworth filter (0.05 filtering frequency, filter order 4) using a custom-written python algorithm. FD curves were fitted using a custom written Python script, which is based on Pylake package provided by Lumicks (https://lumicks-pylake.readthedocs.io/). Scripts have been deposited to GitHub [https://github.com/REMI-HIRI/EMCV_2A_project]. The fitting procedure was done as described[70]. In brief, first, a fully folded part (until the first detectable unfolding step) was fitted with a worm-like chain model (WLC)[71,72] to determine the persistence length (dsL_P) of the tether while the contour length (dsL_C) parameter was held fixed at 1256 nm (± 1%; 4110 bp*0.305 nm/bp and 4 ss*0.59 nm/ss)[73]. The (partially) unfolded parts of FD curve were then fitted by a model comprising of WLC (describing the folded double stranded handles) and a second WLC model (describing the unfolded single stranded parts)[71,74]. For fitting of the unfolded regions, parameters extracted from the fully folded part fitting (dsL_P, dsL_C, dsK) were used and fixed in the WLC part of the combined model. Persistence length of the single stranded part (ssL_P) was fixed at 1 nm while contour length (ssL_C) of the single stranded part

together with the single stranded stretch modulus (ssK) were optimized. The work performed on the structure while unfolding or refolding was calculated as difference between area under curve (AUC) of the fit for the folded region and AUC of the fit for the unfolded region, counted from the beginning of the FD curve till the unfolding step coordinates[75]. If the unfolding and refolding work distributions were overlapping, Crook's fluctuation theorem was applied to estimate the equilibrium work, which represents free Gibbs energy[75], as intersection between the unfolding and refolding work distributions. Since Crooks fluctuation theorem directly averages work values of unfolding and folding, it is not reliable when system is far from equilibrium or in other cases when folding and unfolding work distributions are very different[33]. In our WT+2A samples, the overlap between folding and unfolding work was not sufficient. Therefore, to more accurately estimate the free energies where large fluctuations exist in work distributions, we applied the Jarzynski's equality as described[34]. We then corrected for the bias in the Jarzynski estimate[76]. Theoretical values of the Gibbs free energies for the predicted RNA structures were obtained using mfold[31]. The FD curves were plotted using Prism 8.0.2 (GraphPad). The RNAstructure software (version 6.2) was also used for prediction of the EMCV RNA element secondary structure[77].

Eukaryotic ribosomal subunit purification

40S and 60S subunits were purified from untreated rabbit reticulocyte lysate (Green Hectares) as previously described[78]. Briefly, ribosomes were pelleted by centrifugation (4°C, 270,000 × g, 4.5 h) and resuspended in 20 mM Tris-HCl pH 7.5, 4.0 mM $MgCl_2$, 50 mM KCl, 2.0 mM DTT. Following treatment with 1.0 mM puromycin and addition of KCl to 0.5 M, 40S and 60S subunits were separated by centrifugation (4°C, 87,000 × g, 16 h) through a sucrose density gradient (10 → 30% sucrose in 20 mM Tris-HCl pH 7.5, 2.0 mM DTT, 4.0 mM $MgCl_2$, 0.5 M KCl). After analysis by SDS-PAGE, uncontaminated fractions were pooled, and exchanged into 20 mM Tris-HCl pH 7.5, 100 mM KCl, 2.0 mM $MgCl_2$, 2.0 mM DTT, 250 mM sucrose using Amicon centrifugal concentrators (4°C,100K MWCO). Ribosome subunits were snap-frozen in liquid nitrogen and stored at -80°C until required.

Ribosome binding assays

Assays were conducted in 50 mM Tris-acetate pH 7.5, 150 mM potassium acetate, 5.0 mM magnesium acetate, 0.25 mM spermidine, 10 mM DTT, 0.1 % v/v Triton X-100. Per 60 µL binding reaction, ribosome subunits were diluted to a final concentration of 0.4 µM, and 2A protein was added in excess to a final concentration of 2.4 µM. Twenty microlitres of this

mixture was retained for SDS-PAGE analysis of the 'input'. The remaining 40 µL was incubated at room temperature for 20 min prior to application to a S200-HR size-exclusion microspin column (Cytiva) that had been pre-equilibrated (4 x 500 µL) in the above buffer by resuspension and centrifugation (300 × g, 30 s). Immediately after application, the eluate was collected by centrifugation (300 × g, 60 s).

Western blot

Samples were analysed by 4–20% gradient SDS-PAGE and transferred to a 0.2 µm nitrocellulose membrane. All subsequent steps were carried out at room temperature. Membranes were blocked (5% w/v milk, PBS, 1 h) before incubation (1 h) with primary antibodies in 5% w/v milk, PBS, 0.1% v/v Tween-20. Membranes were washed three times with PBS, 0.1% v/v Tween-20 prior to incubation (1 h) with IRDye fluorescent antibodies in 5% w/v milk, PBS, 0.1% v/v Tween-20. After three washes in PBS, 0.1% v/v Tween-20 and a final rinse in PBS, membranes were imaged using an Odyssey CLx Imaging System (LI-COR). Figures were prepared using ImageStudio Lite 5.2 (LI-COR). Antibodies used were rabbit polyclonal anti-2A[12] (1/1000); mouse monoclonal anti-RPS6 (1/1000, clone A16009C, BioLegend); mouse monoclonal anti-RPL4 (1/1000, clone 4A3, Sigma); goat anti-rabbit IRDye 800 CW (1/10,000, LI-COR) and goat anti-mouse IRDye 680LT (1/10,000, LI-COR). Raw, uncropped blots are available in the **Source Data** file.

In vitro transcription

For *in vitro* frameshifting assays, we cloned a 105 nt DNA fragment (pdluc/EMCV, **Supplementary Table 5**) containing the EMCV slippery sequence flanked by 12 nt upstream and 86 nt downstream into the dual luciferase plasmid pDluc at the XhoI and BglII sites[79]. This sequence was inserted between the Renilla and firefly luciferase genes such that firefly luciferase expression is dependent on −1 PRF. Wild-type or mutated frameshift reporter plasmids were linearized with FspI and capped run-off transcripts generated using T7 RNA polymerase as described[80]. Messenger RNAs were recovered by phenol/chloroform extraction (1:1 v/v), desalted by centrifugation through a NucAway Spin Column (Ambion) and concentrated by ethanol precipitation. The mRNA was resuspended in water, checked for integrity by agarose gel electrophoresis, and quantified by spectrophotometry.

Messenger RNAs for 70S IC preparation (EMCV_IC, **Supplementary Table 5**) were produced from a 117 nt long DNA fragment containing the EMCV frameshift site flanked by the bacterial 5′ UTR with Shine-Dalgarno sequence and 18 nt downstream region of the putative structure.

5′GGGAAUUCAAAAAUUGUUAAGAAUUAAGGAGAUAUACAUAUGGA**GGUUUUU**AUCACUCAA
GGAGCGGCAGUGUCAUCAAUGGCUCAAACCCUACUGCCGAACGACUUGGCCAGATCT 3′

(slippery sequence in bold, initiation codon underlined)

This sequence was PCR amplified and *in vitro* transcribed using T7 RNA polymerase (produced in-house). Messenger RNAs were purified using the Qiagen RNeasy midiprep kit according to the manufacturer's protocols. The mRNAs were eluted in RNAse-free water, integrity and purity was checked by gel electrophoresis and quantified by spectrophotometry.

70S initiation complex preparation

Ribosomes, translation factors, and tRNAs were of *E. coli* origin. Total *E. coli* tRNA was from Roche, and oligonucleotides were from Microsynth. 70*S* ribosomes from MRE600, EF-Tu, EF-G, IF1, IF2 and IF3 were purified from *E. coli* [81]. fMet-tRNA^{fMet} was prepared and aminoacylated according to published protocols[82,83]. Aminoacylated fMet-tRNA^{fMet} was purified by reversed-phase HPLC on a Wide Pore C5 (10 µM particle size 10 mm x 25 cm) column (Sigma Aldrich). To prepare initiation complexes, 70S ribosomes (1 µM) were incubated with a three-fold excess of an EMCV model mRNA (EMCV_IC, **Supplementary Table 5**) encoding for 5′…AUGGA**GGUUUUU**AUC…3′ (slippery sequence in bold) and a 1.5- fold excess each of IF1, IF2, IF3, and fMet-tRNA^{fMet} in buffer A (50 mM Tris-HCl pH 7.5, 70 mM NH_4Cl, 30 mM KCl, 7 mM $MgCl_2$) supplemented with GTP (1 mM) for 30 min at 37°C. 70S initiation complexes were purified by centrifugation through a 1.1 M sucrose cushion in buffer A. Before grid preparation, initiation complexes were additionally purified on Sephacryl S-300 gel filtration microspin columns.

Frameshifting assays (In vitro translation)

Messenger RNAs were translated in nuclease-treated rabbit reticulocyte lysate (RRL) or wheat germ (WG) extracts (Promega). Typical reactions were composed of 90% v/v RRL, 20 µM amino acids (lacking methionine) and 0.2 MBq [^{35}S]-methionine and programmed with ~50 µg/mL template mRNA. Reactions were incubated for 1 h at 30°C. Samples were mixed with 10 volumes of 2× Laemmli's sample buffer, boiled for 3 min and resolved by SDS-PAGE. Dried gels were exposed to a Storage Phosphor Screen (PerkinElmer) and the screen scanned in a Typhoon FLA7000 using phosphor autoradiography mode. Bands were quantified using ImageQuant™TL 8.1.0 software (GE Healthcare). The calculations of frameshifting efficiency (%FS) took into account the differential methionine content of the various products and %FS

was calculated as % –1FS = 100 × (IFS/MetFS) / (IS/MetS + IFS/MetFS). In the formula, the number of methionines in the stop and frameshift products are denoted by MetS, MetFS respectively; while the densitometry values for the same products are denoted by IS and IFS respectively. All frameshift assays were carried out a minimum of three times.

Ribosomal frameshift assays in *E. coli* employed a coupled T7/S30 *in vitro* translation system (Promega). A ~450 bp fragment containing the EMCV PRF signal (or mutant derivative) was prepared by PCR from plasmid pDluc/EMCV[12] and cloned into the BamHI site of the T7-based, *E. coli* expression vector pET3xc[84]. T7/S30 reaction mixes were prepared according to the manufacturer's instructions (50 µL volumes), including 10 µCi ^{35}S methionine, supplemented with plasmid DNA (4 µg) and incubated at 37 ˚C for 90 mins. Reactions were precipitated by addition of an equal volume of acetone, dissolved in Laemmli's sample buffer and aliquots analysed by SDS-PAGE. PRF efficiencies were calculated as above.

Cryo-EM specimen preparation

Initiated 70S ribosomes in 50 mM Tris-HCl pH 7.5, 70 mM NH_4Cl, 30 mM KCl, 7 mM $MgCl_2$ were diluted tenfold into 20 mM HEPES pH 7.5, 100 mM potassium acetate, 1.5 mM $MgCl_2$, 2.0 mM DTT. 2A protein was dialysed (3K MWCO, 4°C, 16 h) into the same buffer. Crosslinking reactions of 50 µL comprising 75 nM ribosomes, 3.0 µM 2A and 2.0 mM bis(sulfosuccinimidyl)suberate (BS3) were performed on ice (30 min) immediately prior to grid preparation. Quantifoil R 2/2 400-mesh copper supports were coated with an additional ~ 60 Å layer of amorphous, evaporated carbon by flotation[85], and thoroughly dried before use. Grids were made hydrophilic by glow-discharge in air for 30 s. Three microliters of crosslinking reaction was applied to grids which were then blotted for 4.5 s and vitrified by plunging into liquid ethane using a Vitrobot MK IV (FEI) at 4°C, 100% relative humidity.

Cryo-EM data collection and processing

Micrographs were collected at the BiocEM facility (Department of Biochemistry, University of Cambridge) on a Titan Krios microscope (FEI) operating at 300 kV and equipped with a Falcon III detector (**Supplementary Table 4**). At 75,000 × magnification, the calibrated pixel size was 1.07 Å / pixel. Per 0.6 s acquisition in integration mode, a total exposure of 54.4 e^- / Å^2 was fractionated over 23 frames with applied defocus of –1.5, –1.8, –2.1, –2.4, –2.7 and –3.0 µm.

EPU software was used for automated acquisition with five images per hole. After manual inspection, 5730 micrographs were used in subsequent image processing.

Movie frames were aligned and a dose-weighted average calculated with MotionCor 2[86]. The contrast transfer function (CTF) was estimated using CtfFind 4[87]. All subsequent image-processing steps were carried out in RELION 3.1[88] (**Supplementary Fig. 6**) and all reported estimates of resolution are based on the gold standard Fourier shell correlation (FSC) at 0.143, and the calculated FSC is derived from comparisons between reconstructions from two independently refined half-sets. Reference-free autopicking of 820,475 particles was performed using the Laplacian-of-Gaussian function (200 - 250 Å diameter). Particles were initially downscaled threefold and extracted in a 150-pixel box. Two rounds of 2D classification (into 100 and 200 classes, respectively) were used to clean the dataset to 750,029 'good' particles. An initial reference was generated from a PDB file of a 70S elongation-competent ribosome (PDB ID 5MDZ [http://doi.org/10.2210/pdb5mdz/pdb]) and low-pass filtered to 80 Å resolution. The initial 3D refinement (6.5 Å resolution) showed clear evidence for at least one copy of 2A adjacent to the factor binding site on the 30S subunit. At this stage, two rounds of focussed classification with signal subtraction were performed (6 classes) to separate particles based on additional density near i) the factor binding site and ii) the mRNA entry channel/helicase. The former was successful and 289,741 particles containing three copies of 2A were rescaled to full size and extracted in a 450-pixel box. Following initial 3D refinement, creation of a 15 Å low-pass filtered mask (five-pixel extension and five-pixel soft edge) and post-processing, a reconstruction of 2.93 Å was achieved. After per-particle CTF refinement and polishing, this was increased to 2.50 Å. With the increased angular accuracy provided by the fully rescaled data, focussed classification with signal subtraction and local angular searches was performed again to separate particles based on 2A occupancy at the factor binding site. This final reconstruction (2.66 Å) from 120,749 particles revealed three copies of 2A bound with full occupancy, and clearer details in the vicinity of the 2A binding sites. Calculation of a local resolution map revealed additional low-resolution density adjacent to the beak of the 30S head. Subsequent focussed classification with signal subtraction and refinement confirmed that this was a fourth copy of 2A bound, present in 73,059 particles.

To build the model, the atomic coordinates for a 70S initiation complex (5MDZ [http://doi.org/10.2210/pdb5mdz/pdb]) and three copies of chain A from the 2A crystal structure (above) were docked as rigid bodies into the EM map. Local rebuilding was

performed iteratively in COOT[63] and the models refined using phenix real-space refine[64] implementing reference model restraints to preserve geometry.

Visualisation of structural data

All structural figures depicting crystallographic data (cartoon, stick and surface representations) were rendered in PyMOL 2.3.4 (Schrödinger LLC). Structural figures of EM maps with docked components were rendered in ChimeraX 1.1[89].

Data Availability

The atomic coordinates and structure factors for the EMCV 2A X-ray crystal structure have been deposited in the wwPDB database under accession code 7BNY [http://doi.org/10.2210/pdb7bny/pdb]. The 70S IC:2A cryo-EM map has been deposited in the EMDB under accession code EMD-12635 [https://www.ebi.ac.uk/emdb/EMD-12257] and the refined atomic coordinates accompanying this structure have been deposited to the wwPDB under accession code 7NWT [http://doi.org/10.2210/pdb7nwt/pdb]. Previously published structures that were used in this study are also available in the wwPDB: 5WE6 [http://doi.org/10.2210/pdb5we6/pdb], 4V7D [http://doi.org/10.2210/pdb4v7d/pdb] and 5MDZ [http://doi.org/10.2210/pdb5mdz/pdb]. Source data are provided with this paper. All raw data (e.g. uncropped, unannotated gels, western blots, tables of force measurements, MST traces) corresponding to individual figure panels are provided in the Source Data File and have also been deposited in Mendeley Data [http://dx.doi.org/10.17632/gkpwngy65h.2].

Code Availability

The force spectroscopy analysis scripts supporting the current study have been uploaded to GitHub [https://github.com/REMI-HIRI/EMCV_2A_project]. Further information is available on request from Neva Caliskan (neva.caliskan@helmholtz-hiri.de).

References

1. Firth, A.E. & Brierley, I. Non-canonical translation in RNA viruses. *J Gen Virol* **93**, 1385-1409 (2012).
2. Atkins, J.F., Loughran, G., Bhatt, P.R., Firth, A.E. & Baranov, P.V. Ribosomal frameshifting and transcriptional slippage: From genetic steganography and cryptography to adventitious use. *Nucleic Acids Res* **44**, 7007-78 (2016).
3. Korniy, N., Samatova, E., Anokhina, M.M., Peske, F. & Rodnina, M.V. Mechanisms and biomedical implications of -1 programmed ribosome frameshifting on viral and bacterial mRNAs. *FEBS Lett* **593**, 1468-1482 (2019).
4. Chen, J. et al. Dynamic pathways of -1 translational frameshifting. *Nature* **512**, 328-32 (2014).
5. Caliskan, N., Katunin, V.I., Belardinelli, R., Peske, F. & Rodnina, M.V. Programmed -1 frameshifting by kinetic partitioning during impeded translocation. *Cell* **157**, 1619-31 (2014).
6. Choi, J., O'Loughlin, S., Atkins, J.F. & Puglisi, J.D. The energy landscape of -1 ribosomal frameshifting. *Sci Adv* **6**, eaax6969 (2020).
7. Namy, O., Moran, S.J., Stuart, D.I., Gilbert, R.J. & Brierley, I. A mechanical explanation of RNA pseudoknot function in programmed ribosomal frameshifting. *Nature* **441**, 244-7 (2006).
8. Giedroc, D.P. & Cornish, P.V. Frameshifting RNA pseudoknots: structure and mechanism. *Virus Res* **139**, 193-208 (2009).
9. Chen, G., Chang, K.Y., Chou, M.Y., Bustamante, C. & Tinoco, I., Jr. Triplex structures in an RNA pseudoknot enhance mechanical stability and increase efficiency of -1 ribosomal frameshifting. *Proc Natl Acad Sci U S A* **106**, 12706-11 (2009).
10. Halma, M.T.J., Ritchie, D.B., Cappellano, T.R., Neupane, K. & Woodside, M.T. Complex dynamics under tension in a high-efficiency frameshift stimulatory structure. *Proc Natl Acad Sci U S A* **116**, 19500-19505 (2019).
11. Loughran, G., Firth, A.E. & Atkins, J.F. Ribosomal frameshifting into an overlapping gene in the 2B-encoding region of the cardiovirus genome. *Proc Natl Acad Sci U S A* **108**, E1111-9 (2011).
12. Napthine, S. et al. Protein-directed ribosomal frameshifting temporally regulates gene expression. *Nat Commun* **8**, 15582 (2017).
13. Jackson, R.J. A detailed kinetic analysis of the in vitro synthesis and processing of encephalomyocarditis virus products. *Virology* **149**, 114-27 (1986).
14. Hahn, H. & Palmenberg, A.C. Deletion mapping of the encephalomyocarditis virus primary cleavage site. *J Virol* **75**, 7215-8 (2001).
15. Yang, X. et al. Structures and Corresponding Functions of Five Types of Picornaviral 2A Proteins. *Front Microbiol* **8**, 1373 (2017).
16. Groppo, R. & Palmenberg, A.C. Cardiovirus 2A protein associates with 40S but not 80S ribosome subunits during infection. *J Virol* **81**, 13067-74 (2007).
17. Carocci, M. et al. Encephalomyocarditis virus 2A protein is required for viral pathogenesis and inhibition of apoptosis. *J Virol* **85**, 10741-54 (2011).
18. Merrick, W.C. eIF4F: a retrospective. *J Biol Chem* **290**, 24091-9 (2015).
19. Krissinel, E. & Henrick, K. Secondary-structure matching (SSM), a new tool for fast protein structure alignment in three dimensions. *Acta Crystallogr D Biol Crystallogr* **60**, 2256-68 (2004).
20. Holm, L. & Laakso, L.M. Dali server update. *Nucleic Acids Res* **44**, W351-5 (2016).
21. Redfern, O.C., Harrison, A., Dallman, T., Pearl, F.M. & Orengo, C.A. CATHEDRAL: a fast and effective algorithm to predict folds and domain boundaries from multidomain protein structures. *PLoS Comput Biol* **3**, e232 (2007).

22. Svitkin, Y.V., Hahn, H., Gingras, A.C., Palmenberg, A.C. & Sonenberg, N. Rapamycin and wortmannin enhance replication of a defective encephalomyocarditis virus. *J Virol* **72**, 5811-9 (1998).
23. Groppo, R., Brown, B.A. & Palmenberg, A.C. Mutational analysis of the EMCV 2A protein identifies a nuclear localization signal and an eIF4E binding site. *Virology* **410**, 257-67 (2011).
24. Petty, R.V., Basta, H.A., Bacot-Davis, V.R., Brown, B.A. & Palmenberg, A.C. Binding interactions between the encephalomyocarditis virus leader and protein 2A. *J Virol* **88**, 13503-9 (2014).
25. Siddiqui, N. et al. Structural insights into the allosteric effects of 4EBP1 on the eukaryotic translation initiation factor eIF4E. *J Mol Biol* **415**, 781-92 (2012).
26. Magnus, M., Boniecki, M.J., Dawson, W. & Bujnicki, J.M. SimRNAweb: a web server for RNA 3D structure modeling with optional restraints. *Nucleic Acids Res* **44**, W315-9 (2016).
27. Ren, J., Rastegari, B., Condon, A. & Hoos, H.H. HotKnots: heuristic prediction of RNA secondary structures including pseudoknots. *RNA* **11**, 1494-504 (2005).
28. Chen, G., Wen, J.D. & Tinoco, I., Jr. Single-molecule mechanical unfolding and folding of a pseudoknot in human telomerase RNA. *RNA* **13**, 2175-88 (2007).
29. Li, P.T., Collin, D., Smith, S.B., Bustamante, C. & Tinoco, I., Jr. Probing the mechanical folding kinetics of TAR RNA by hopping, force-jump, and force-ramp methods. *Biophys J* **90**, 250-60 (2006).
30. Heller, I., Hoekstra, T.P., King, G.A., Peterman, E.J. & Wuite, G.J. Optical tweezers analysis of DNA-protein complexes. *Chem Rev* **114**, 3087-119 (2014).
31. Zuker, M. Mfold web server for nucleic acid folding and hybridization prediction. *Nucleic Acids Res* **31**, 3406-15 (2003).
32. Ritchie, D.B., Foster, D.A. & Woodside, M.T. Programmed -1 frameshifting efficiency correlates with RNA pseudoknot conformational plasticity, not resistance to mechanical unfolding. *Proc Natl Acad Sci U S A* **109**, 16167-72 (2012).
33. Mangeol, P. et al. Probing ribosomal protein-RNA interactions with an external force. *Proc Natl Acad Sci U S A* **108**, 18272-6 (2011).
34. Liphardt, J., Dumont, S., Smith, S.B., Tinoco, I., Jr. & Bustamante, C. Equilibrium information from nonequilibrium measurements in an experimental test of Jarzynski's equality. *Science* **296**, 1832-5 (2002).
35. Leger, M., Sidani, S. & Brakier-Gingras, L. A reassessment of the response of the bacterial ribosome to the frameshift stimulatory signal of the human immunodeficiency virus type 1. *RNA* **10**, 1225-35 (2004).
36. Horsfield, J.A., Wilson, D.N., Mannering, S.A., Adamski, F.M. & Tate, W.P. Prokaryotic ribosomes recode the HIV-1 gag-pol-1 frameshift sequence by an E/P site post-translocation simultaneous slippage mechanism. *Nucleic Acids Res* **23**, 1487-94 (1995).
37. James, N.R., Brown, A., Gordiyenko, Y. & Ramakrishnan, V. Translational termination without a stop codon. *Science* **354**, 1437-1440 (2016).
38. Brilot, A.F., Korostelev, A.A., Ermolenko, D.N. & Grigorieff, N. Structure of the ribosome with elongation factor G trapped in the pretranslocation state. *Proc Natl Acad Sci U S A* **110**, 20994-9 (2013).
39. Lin, J., Gagnon, M.G., Bulkley, D. & Steitz, T.A. Conformational changes of elongation factor G on the ribosome during tRNA translocation. *Cell* **160**, 219-27 (2015).
40. Bulkley, D. et al. The antibiotics dityromycin and GE82832 bind protein S12 and block EF-G-catalyzed translocation. *Cell Rep* **6**, 357-65 (2014).
41. Fislage, M. et al. Cryo-EM shows stages of initial codon selection on the ribosome by aa-tRNA in ternary complex with GTP and the GTPase-deficient EF-TuH84A. *Nucleic Acids Res* **46**, 5861-5874 (2018).
42. Loveland, A.B., Demo, G. & Korostelev, A.A. Cryo-EM of elongating ribosome with EF-Tu*GTP elucidates tRNA proofreading. *Nature* (2020).

43. Hussain, T., Llacer, J.L., Wimberly, B.T., Kieft, J.S. & Ramakrishnan, V. Large-Scale Movements of IF3 and tRNA during Bacterial Translation Initiation. *Cell* **167**, 133-144 e13 (2016).
44. Napthine, S., Bell, S., Hill, C.H., Brierley, I. & Firth, A.E. Characterization of the stimulators of protein-directed ribosomal frameshifting in Theiler's murine encephalomyelitis virus. *Nucleic Acids Res* **47**, 8207-8223 (2019).
45. Wen, J.D. et al. Following translation by single ribosomes one codon at a time. *Nature* **452**, 598-603 (2008).
46. Kim, H.K. et al. A frameshifting stimulatory stem loop destabilizes the hybrid state and impedes ribosomal translocation. *Proc Natl Acad Sci U S A* **111**, 5538-43 (2014).
47. Qin, P., Yu, D., Zuo, X. & Cornish, P.V. Structured mRNA induces the ribosome into a hyper-rotated state. *EMBO Rep* **15**, 185-90 (2014).
48. Bao, C. et al. mRNA stem-loops can pause the ribosome by hindering A-site tRNA binding. *Elife* **9**(2020).
49. Yang, L. et al. Single-Molecule Mechanical Folding and Unfolding of RNA Hairpins: Effects of Single A-U to A.C Pair Substitutions and Single Proton Binding and Implications for mRNA Structure-Induced -1 Ribosomal Frameshifting. *J Am Chem Soc* **140**, 8172-8184 (2018).
50. Zhong, Z. et al. Mechanical unfolding kinetics of the SRV-1 gag-pro mRNA pseudoknot: possible implications for -1 ribosomal frameshifting stimulation. *Sci Rep* **6**, 39549 (2016).
51. Bock, L.V. et al. Thermodynamic control of -1 programmed ribosomal frameshifting. *Nat Commun* **10**, 4598 (2019).
52. Peng, B.Z. et al. Active role of elongation factor G in maintaining the mRNA reading frame during translation. *Sci Adv* **5**, eaax8030 (2019).
53. Neidel, S. et al. Vaccinia virus protein A49 is an unexpected member of the B-cell Lymphoma (Bcl)-2 protein family. *J Biol Chem* **290**, 5991-6002 (2015).
54. Winter, G. *xia2*: an expert system for macromolecular crystallography data reduction. *J. Appl. Cryst.* **43**, 186-190 (2009).
55. Kabsch, W. XDS. *Acta Crystallogr D Biol Crystallogr* **66**, 125-32 (2010).
56. Evans, P.R. & Murshudov, G.N. How good are my data and what is the resolution? *Acta Crystallogr D Biol Crystallogr* **69**, 1204-14 (2013).
57. Karplus, P.A. & Diederichs, K. Linking crystallographic model and data quality. *Science* **336**, 1030-3 (2012).
58. Vonrhein, C., Blanc, E., Roversi, P. & Bricogne, G. Automated structure solution with autoSHARP. *Methods Mol Biol* **364**, 215-30 (2007).
59. Sheldrick, G.M. A short history of SHELX. *Acta Crystallogr A* **64**, 112-22 (2008).
60. Abrahams, J.P. & Leslie, A.G. Methods used in the structure determination of bovine mitochondrial F1 ATPase. *Acta Crystallogr D Biol Crystallogr* **52**, 30-42 (1996).
61. Perrakis, A., Harkiolaki, M., Wilson, K.S. & Lamzin, V.S. ARP/wARP and molecular replacement. *Acta Crystallogr D Biol Crystallogr* **57**, 1445-50 (2001).
62. McCoy, A.J. et al. Phaser crystallographic software. *J Appl Crystallogr* **40**, 658-674 (2007).
63. Emsley, P., Lohkamp, B., Scott, W.G. & Cowtan, K. Features and development of Coot. *Acta Crystallogr D Biol Crystallogr* **66**, 486-501 (2010).
64. Adams, P.D. et al. PHENIX: a comprehensive Python-based system for macromolecular structure solution. *Acta Crystallogr D Biol Crystallogr* **66**, 213-21 (2010).
65. Chen, V.B. et al. MolProbity: all-atom structure validation for macromolecular crystallography. *Acta Crystallogr D Biol Crystallogr* **66**, 12-21 (2010).
66. Dolinsky, T.J., Nielsen, J.E., McCammon, J.A. & Baker, N.A. PDB2PQR: an automated pipeline for the setup of Poisson-Boltzmann electrostatics calculations. *Nucleic Acids Res* **32**, W665-7 (2004).

67. Baker, N.A., Sept, D., Joseph, S., Holst, M.J. & McCammon, J.A. Electrostatics of nanosystems: application to microtubules and the ribosome. *Proc Natl Acad Sci U S A* **98**, 10037-41 (2001).
68. Krissinel, E. & Henrick, K. Inference of macromolecular assemblies from crystalline state. *J Mol Biol* **372**, 774-97 (2007).
69. Stephenson, W., Wan, G., Tenenbaum, S.A. & Li, P.T. Nanomanipulation of single RNA molecules by optical tweezers. *J Vis Exp* (2014).
70. Mukhortava, A. et al. Structural heterogeneity of attC integron recombination sites revealed by optical tweezers. *Nucleic Acids Res* **47**, 1861-1870 (2019).
71. Wang, M.D., Yin, H., Landick, R., Gelles, J. & Block, S.M. Stretching DNA with optical tweezers. *Biophys J* **72**, 1335-46 (1997).
72. Odijk, T. Stiff Chains and Filaments under Tension. *Macromolecules* **28**, 7016-7018 (1995).
73. Zhang, C. et al. The Mechanical Properties of RNA-DNA Hybrid Duplex Stretched by Magnetic Tweezers. *Biophys J* **116**, 196-204 (2019).
74. Smith, S.B., Cui, Y. & Bustamante, C. Overstretching B-DNA: the elastic response of individual double-stranded and single-stranded DNA molecules. *Science* **271**, 795-9 (1996).
75. McCauley, M.J., Rouzina, I., Li, J., Nunez, M.E. & Williams, M.C. Significant Differences in RNA Structure Destabilization by HIV-1 GagDp6 and NCp7 Proteins. *Viruses* **12**(2020).
76. Gore, J., Ritort, F. & Bustamante, C. Bias and error in estimates of equilibrium free-energy differences from nonequilibrium measurements. *Proc Natl Acad Sci U S A* **100**, 12564-9 (2003).
77. Bellaousov, S., Reuter, J.S., Seetin, M.G. & Mathews, D.H. RNAstructure: Web servers for RNA secondary structure prediction and analysis. *Nucleic Acids Res* **41**, W471-4 (2013).
78. Pisarev, A.V., Unbehaun, A., Hellen, C.U. & Pestova, T.V. Assembly and analysis of eukaryotic translation initiation complexes. *Methods Enzymol* **430**, 147-77 (2007).
79. Fixsen, S.M. & Howard, M.T. Processive selenocysteine incorporation during synthesis of eukaryotic selenoproteins. *J Mol Biol* **399**, 385-96 (2010).
80. Powell, M.L., Brown, T.D. & Brierley, I. Translational termination-re-initiation in viral systems. *Biochem Soc Trans* **36**, 717-22 (2008).
81. Milon, P. et al. Transient kinetics, fluorescence, and FRET in studies of initiation of translation in bacteria. *Methods Enzymol* **430**, 1-30 (2007).
82. Rodnina, M.V., Semenkov, Y.P. & Wintermeyer, W. Purification of fMet-tRNA(fMet) by fast protein liquid chromatography. *Anal Biochem* **219**, 380-1 (1994).
83. Kothe, U., Paleskava, A., Konevega, A.L. & Rodnina, M.V. Single-step purification of specific tRNAs by hydrophobic tagging. *Anal Biochem* **356**, 148-50 (2006).
84. Studier, F.W., Rosenberg, A.H., Dunn, J.J. & Dubendorff, J.W. Use of T7 RNA polymerase to direct expression of cloned genes. *Methods Enzymol* **185**, 60-89 (1990).
85. Passmore, L.A. & Russo, C.J. Specimen Preparation for High-Resolution Cryo-EM. *Methods Enzymol* **579**, 51-86 (2016).
86. Zheng, S.Q. et al. MotionCor2: anisotropic correction of beam-induced motion for improved cryo-electron microscopy. *Nat Methods* **14**, 331-332 (2017).
87. Rohou, A. & Grigorieff, N. CTFFIND4: Fast and accurate defocus estimation from electron micrographs. *J Struct Biol* **192**, 216-21 (2015).
88. Zivanov, J. et al. New tools for automated high-resolution cryo-EM structure determination in RELION-3. *Elife* **7**(2018).
89. Pettersen, E.F. et al. UCSF Chimera--a visualization system for exploratory research and analysis. *J Comput Chem* **25**, 1605-12 (2004).

Acknowledgements

We thank Dima Chirgadze, Steve Hardwick and Lee Cooper (BiocEM facility) for assistance with CryoEM data acquisition. We thank Ann Mukhortava and Bärbel Lorenz (Lumicks AG) for technical assistance with optical tweezer experiments and Ann Mukhortava for critical reading of the manuscript. We thank Prof. Marina V. Rodnina for providing expression constructs. We thank Matthias Zimmer, Trevor Sweeney, Janet Deane and Tatyana Koch for experimental assistance. We thank Vish Chandrasekaran, Jailson Brito Querido, Sebastian Kraatz and Chris Rae for helpful discussions. A Titan V graphics card used for this research was donated by the NVIDIA Corporation. Remote synchrotron access was supported in part by the EU FP7 infrastructure grant BIOSTRUCT-X (Contract No. 283570). We thank the staff of Diamond Light Source beamline I03 for assistance with crystal screening and data collection. Part of this work was carried out in the laboratory of V. Ramakrishnan, who was funded by the UK Medical Research Council (MC_U105184332), and a Wellcome Trust Senior Investigator award (WT096570). CHH and SN were supported by a Wellcome Trust Investigator Award (202797/Z/16/Z) to IB. CHH is funded by a Sir Henry Dale fellowship (221818/Z/20/Z) from the Wellcome Trust and the Royal Society. AEF is supported by Wellcome Trust (106207/Z/14/Z) and European Research Council (646891) grants to AEF. SCG is funded by a Sir Henry Dale fellowship (098406/Z/12/B) from the Wellcome Trust and the Royal Society. NC, LP and AK are supported by the Helmholtz Association. NC is funded by the European Research Council StG (948636).

Author Contributions

C.H.H. and S.N. cloned expressed and purified proteins and performed most of the biochemical experiments. L.P. designed OT constructs and performed single-molecule optical tweezers experiments and analyses under the supervision of N.C. C.H.H. and S.C.G performed crystallography experiments. A.K. and N.C. performed MST experiments and analyses. N.C. prepared and purified bacterial initiation complexes for structural analysis. C.H.H. prepared cryo-EM grids and collected and processed cryo-EM data. C.H.H., S.N., A.F., N.C. and I.B. wrote the manuscript with contributions from all authors.

Competing Interests

The authors declare no competing interests.

Figures

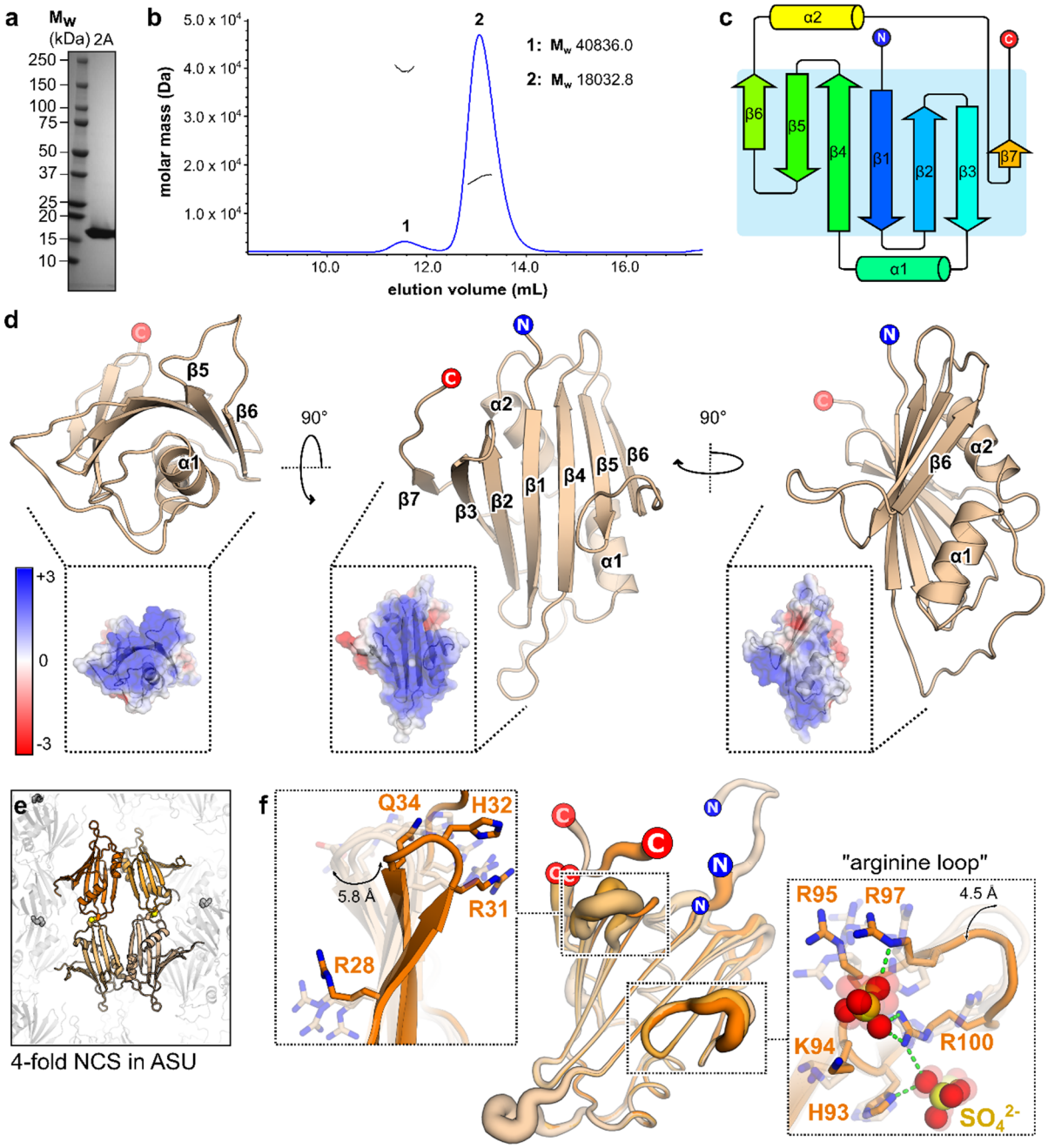

Figure 1. 2A adopts a highly basic RNA-binding fold with intrinsic flexibility. a, SDS-PAGE analysis of EMCV 2A (Coomassie). Representative gel from five independent purifications. **b,** SEC-MALS analysis of 2A. The differential refractive index is shown across the elution profile (blue) and weight-averaged molar masses of the indicated peaks are listed. **c,** Topological diagram of "beta-shell" fold: a curved central sheet comprising seven antiparallel beta strands, supported by two helices. **d,** Crystal structure of EMCV 2A in three orthogonal views. N- and C- termini are indicated. <*Inset*> Electrostatic surface potential

calculated at pH 7.4, coloured between +3 (blue) and -3 (red) kT/e^-. **e,** Four molecules of 2A are present in the asymmetric unit of the crystal, arranged as two pairs of disulfide-linked dimers (spheres). **f,** Superposition of the four NCS-related 2A chains in **e** reveals regions of conformational flexibility. The width of the cartoon is proportional to atomic B-factor. *<Insets>* Close-up view of surface loops exhibiting the greatest variation per molecule. Flexible sidechains are shown as sticks, and the Cα backbone deviation is indicated in Å. The positions of two sulfate ions from the crystallisation buffer are indicated with spheres. Source data are provided as a Source Data file.

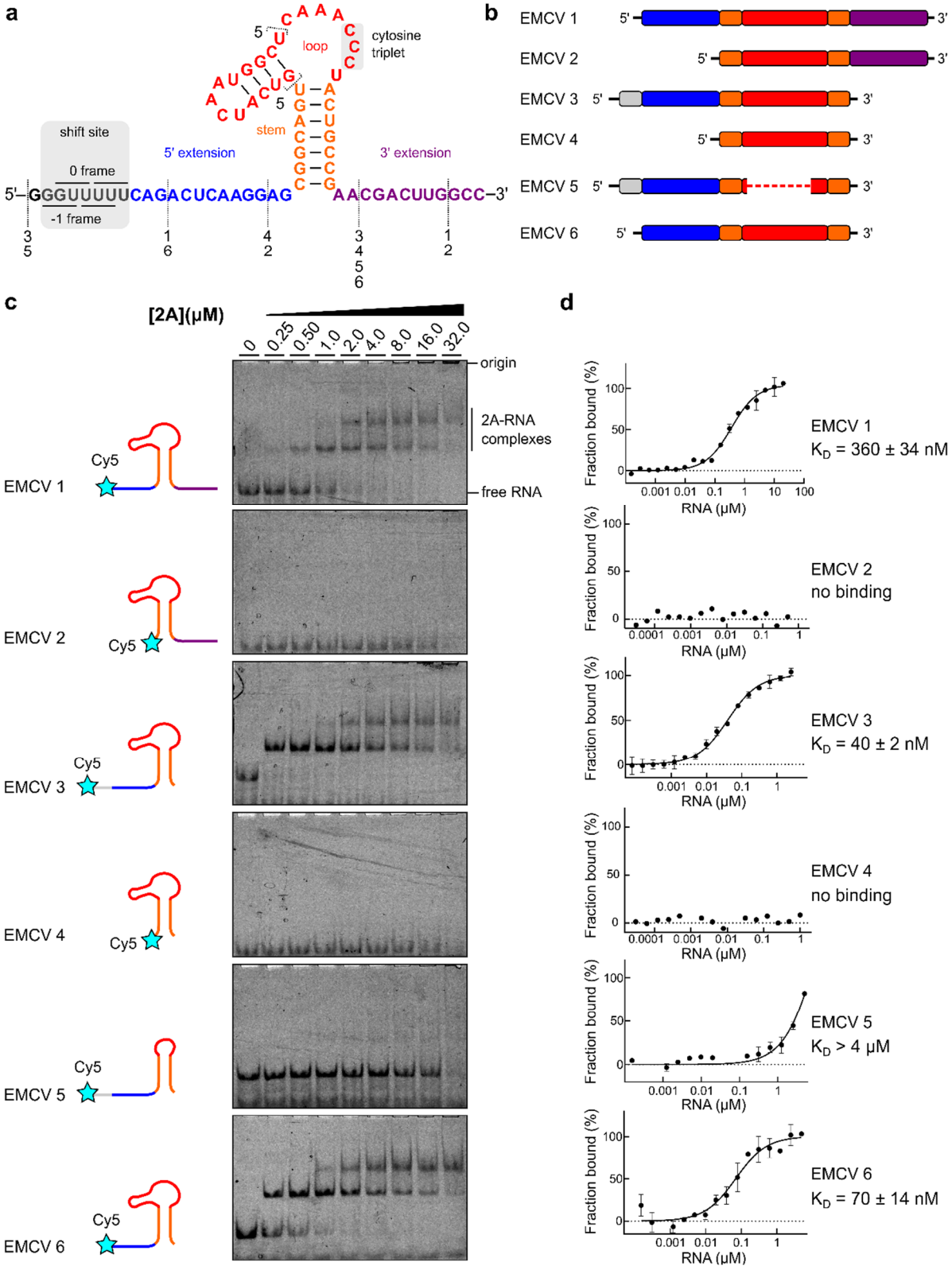

Figure 2. 2A binds to a minimal 47 nt element in the viral RNA. a-b, Sequences and schematic diagrams of the EMCV 1–6 constructs used to assay 2A binding. **c,** EMSA analyses showing that removal of the 5′ extension (blue) disables 2A binding. **d,** Microscale thermophoresis (MST) was used to quantify the interactions observed in **c**. All measurements

were repeated as two independent experiments and error bars represent the standard deviation from the mean. RNA concentration ranges between 60 pM – 20 µM (for EMCV 1) and 150 pM – 5 µM (for EMCV 2–6). Source data are provided as a Source Data file.

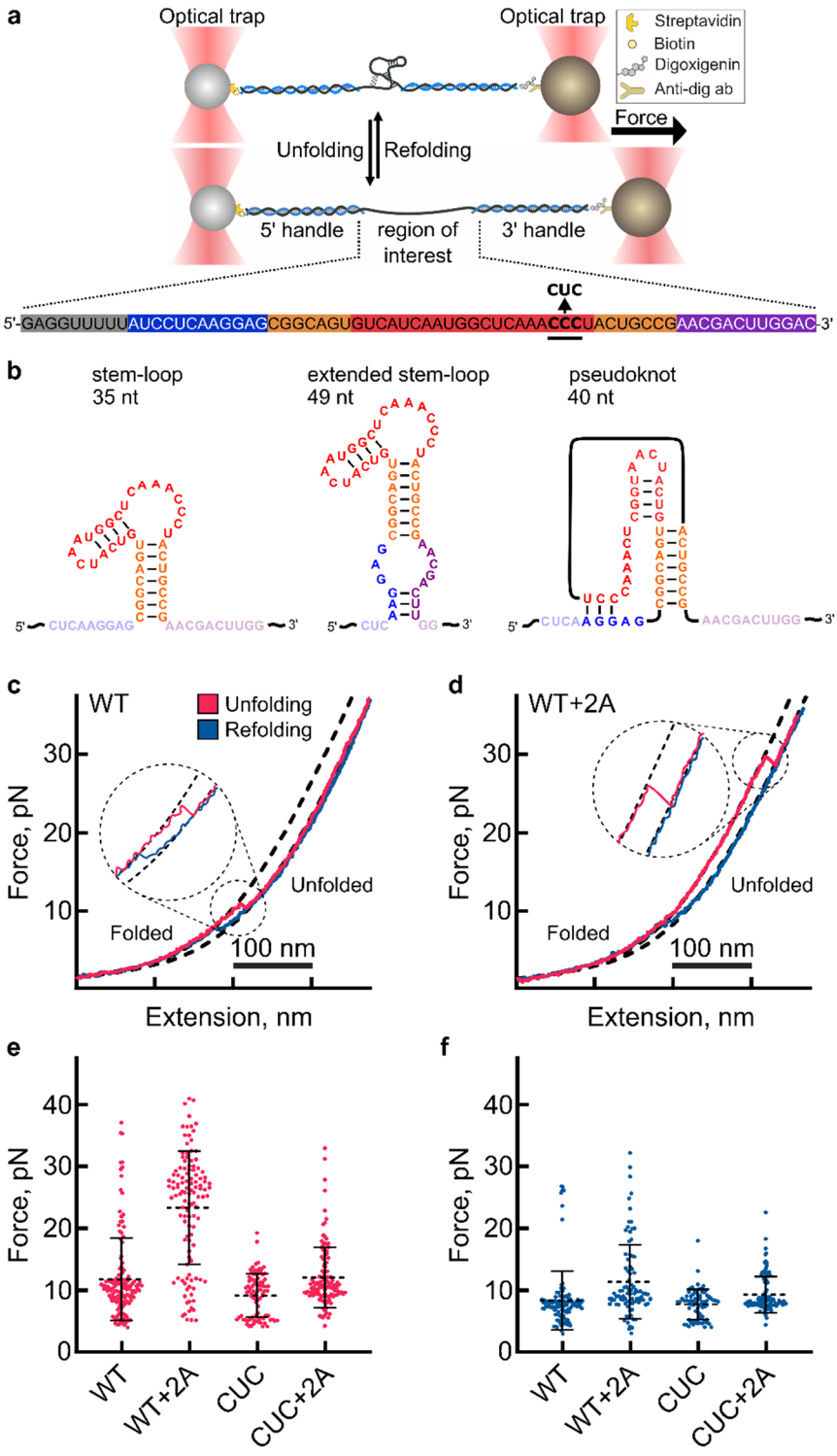

Figure 3. Conformations of EMCV frameshifting RNA and effect of 2A on RNA unwinding. a, <*Upper*> Schematic diagram illustrating the optical tweezer experiments (right). RNA is hybridized to ssDNA handles and immobilised on beads. These are used to exert pulling force on the RNA with a focused laser beam. <*Lower*> Primary sequence of the construct used in optical tweezer experiments, colour coded as in **Fig. 2**. The location of the cytosine triplet (wild-type, WT) and point mutation (CUC) is indicated. **b,** Predicted

conformations of the RNA construct in a. The number of nucleotides involved in each folded structure is indicated. Also see **Supplementary Table S6**. **c,** Representative force-distance curves of the unfolding (pink) and refolding (blue) transitions of the wild type (WT) CCC RNA element. **d,** Representative force-distance curves of the unfolding (pink) and refolding (blue) transitions of the wild type (WT) CCC RNA element in the presence of 300 nM 2A protein. **e**, Global analysis of all the unfolding force trajectories. Number of individual measurements are WT=117, WT+2A=104, CUC=85, CUC+2A=109. Data (black line) are presented as mean values ± SD error bars. **f**, Global analysis of all refolding force trajectories. Number of individual measurements are WT=111, WT+2A=89, CUC=74, CUC+2A=97. Data (black line) are presented as mean values ± SD error bars. Source data are provided as a Source Data file.

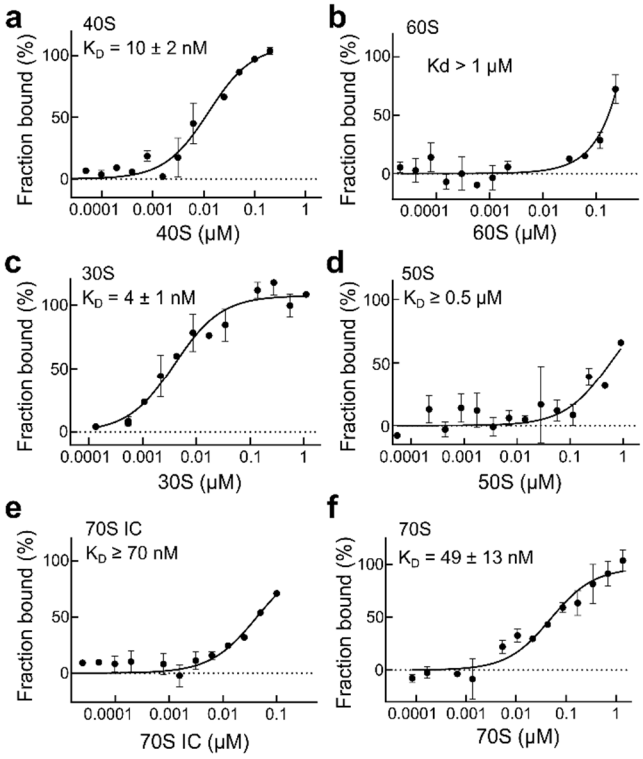

Figure 4. 2A binds directly to eukaryotic and prokaryotic ribosomes. a, MST binding curves and apparent K_D values using unlabelled 40S subunits at a concentration range of 20 pM – 0.4 μM. All measurements were repeated as two independent experiments and error bars represent the standard deviation from the mean. 2A binds with high affinity to the small ribosomal subunit. **b,** As in **a** with 60S subunits. Error bars as above. **c,** Binding curve and apparent K_D values using unlabelled 30S subunits at a concentration range of 30 pM – 1 μM. Error bars as above. 2A shows a strong interaction with the prokaryotic small subunit. **d,** As in **c** with 50S subunits at a concentration range of 27 pM – 0.9 μM. **e,** Binding curves and reported K_D values for 2A-70S IC interactions. Error bars as above. **f,** Same as **e**, with 2A and vacant 70S. Source data are provided as a Source Data file.

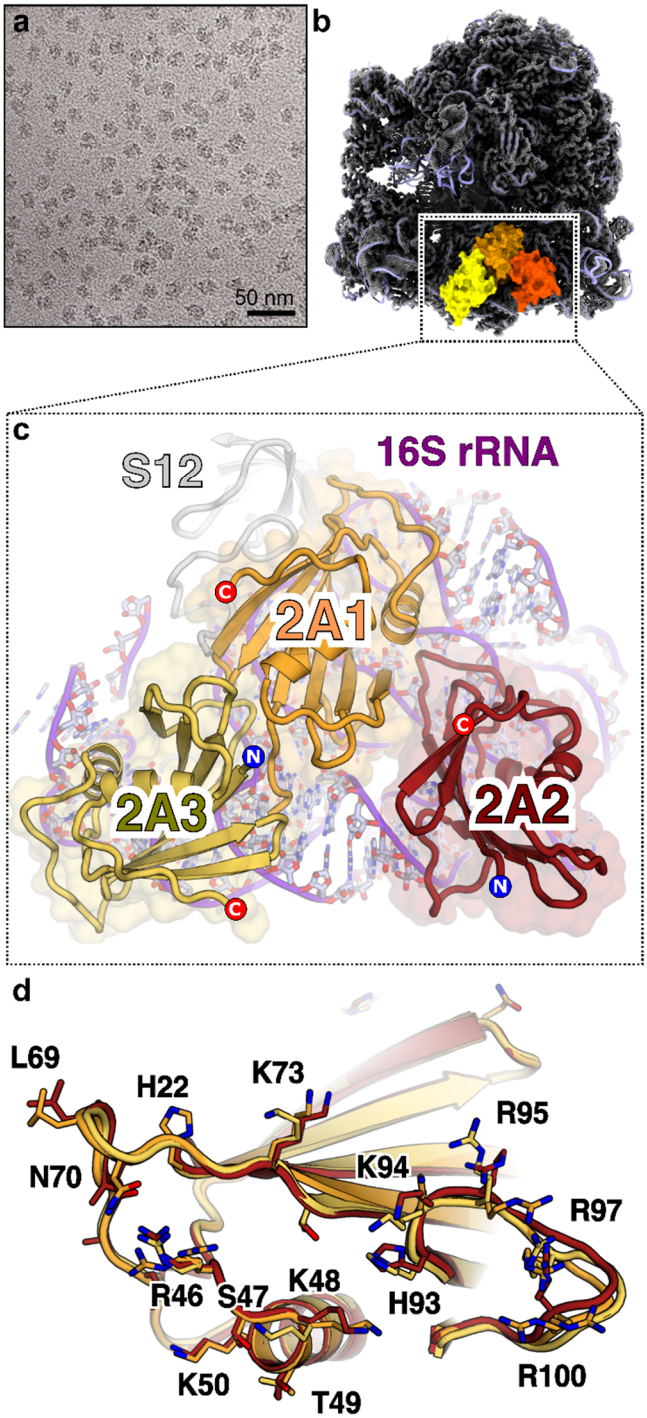

Figure 5. 2A binds to the 70S ribosome via interactions with the 16S rRNA. a, Cryo-EM analysis of a complex formed between initiated *E. coli* 70S ribosomes and EMCV 2A. Images (× 75,000) were recorded on a Titan Krios microscope. Representative micrograph from dataset of 5730 images. **b,** Cryo-EM map at 2.7 Å resolution after focused classification and refinement. Three copies of 2A (orange, red, yellow) are bound to the 16S rRNA of the small (30S) subunit (blue ribbon). **c**, Close-up view of the 2A binding site. Ribbon diagrams of 2A (coloured as above) and ribosomal RNA (purple) are shown. Protein N- and C- termini are labelled. **d,** Superposition of the three copies of 2A reveals a common RNA-binding surface

with conformational flexibility. Residues involved in rRNA binding are labelled and shown as sticks.

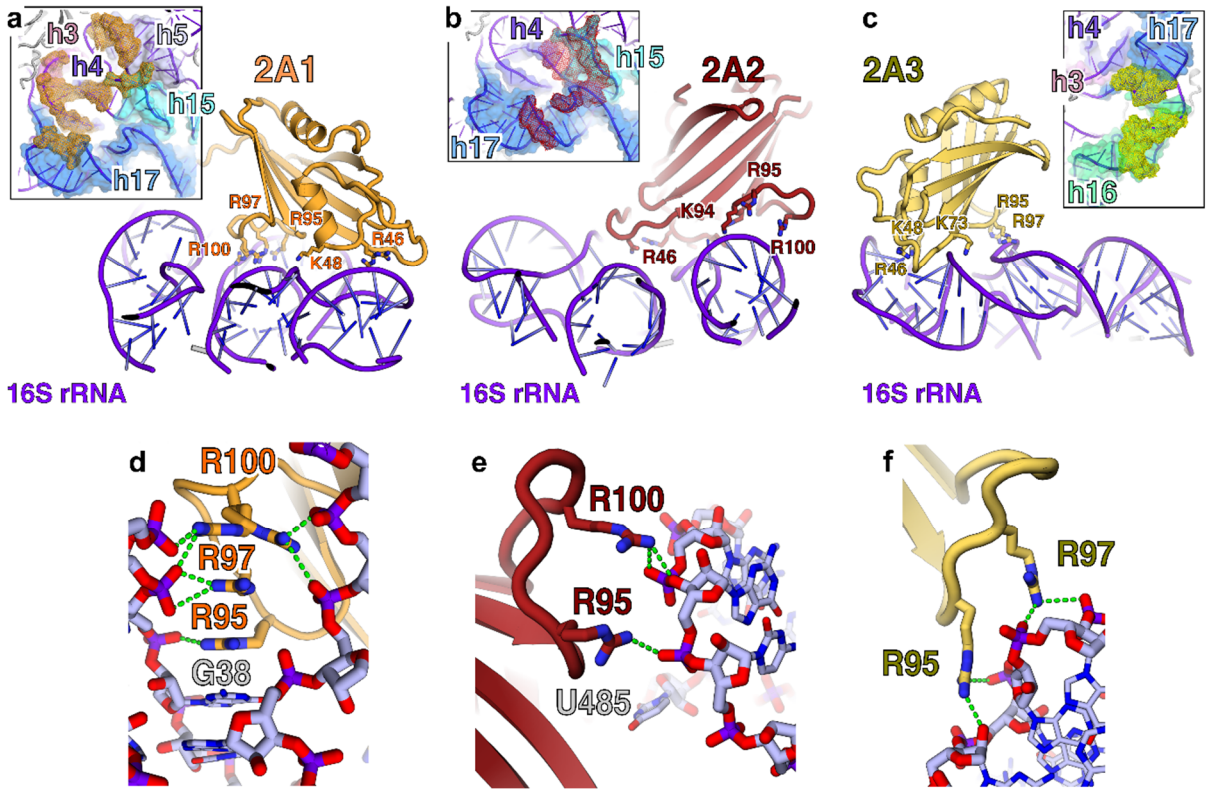

Figure 6. The 'arginine loop' plays a central role in RNA recognition. a-c, Details of rRNA recognition by 2A. For each copy of 2A, selected residues involved in interactions are labelled and shown as sticks <*Insets*> View of the rRNA surface bound by each copy of 2A. The rRNA helices are colour-coded and labelled. The 2A contact surface is shown as a coloured mesh (orange, red and yellow, respectively). **d–f,** Close-up view of interactions between the 2A 'arginine loop' residues (R95, R97 and R100) and the rRNA backbone (sticks) for each copy of 2A (orange, red, yellow). Polar or electrostatic contacts are indicated by a green dashed line.

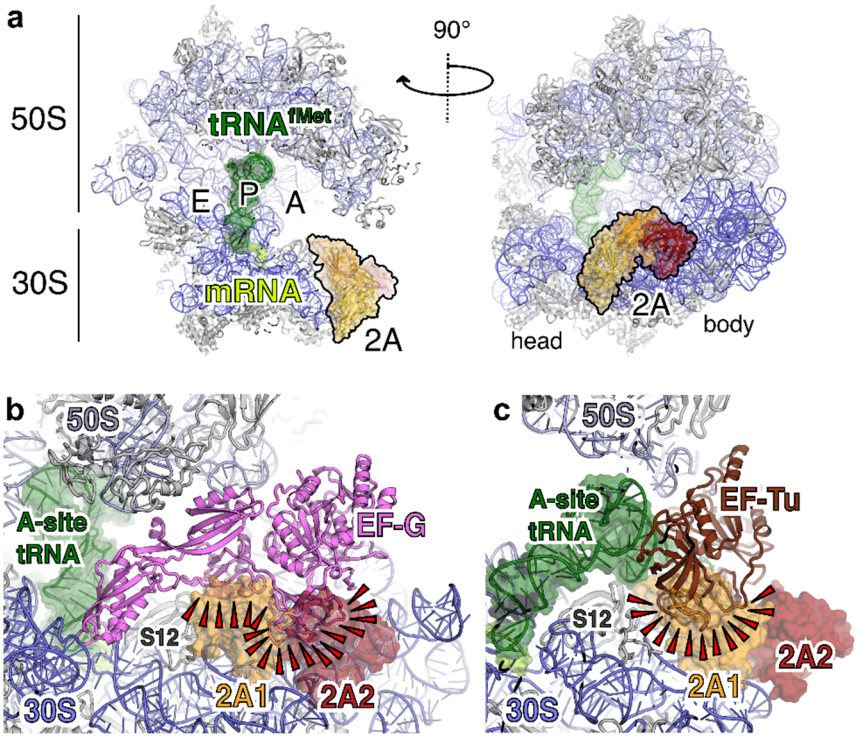

Figure 7. 2A binding may clash with translational GTPases. a, Ribbon diagram of initiated 70S-mRNA-tRNA^{fMet}-2A complex. Ribosome sites are labelled A, P and E. The initiator tRNA^{fMet} (dark green), mRNA (light green), and 2A (orange, red, yellow) are shown in two orthogonal views. **b,** Comparison of 70S-2A complex to 70S pre-translocation complex with EF-G (4V7D [http://doi.org/10.2210/pdb4v7d/pdb]). 2A binding would clash (red wedges) with EF-G binding. **c,** Comparison of 70S-2A complex to 70S complex with EF-Tu (5WE6 [http://doi.org/10.2210/pdb5we6/pdb]). 2A binding would clash (red wedges) with EF-Tu binding.

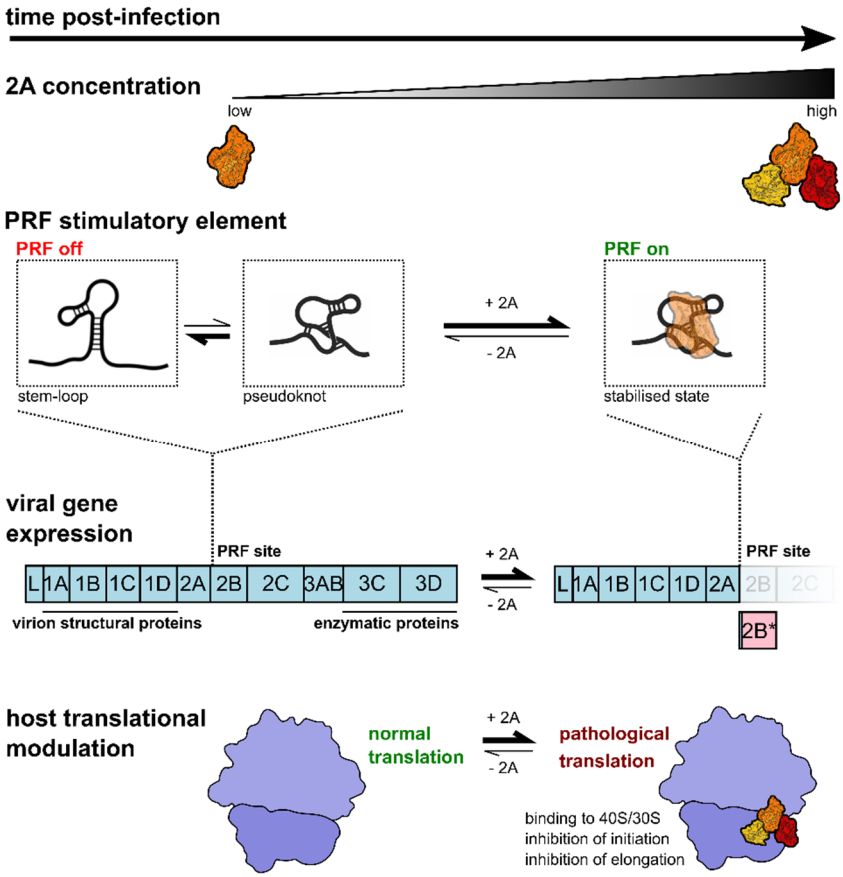

Figure 8. Molecular basis for 2A-induced reprogramming of gene expression. The PRF stimulatory RNA element is predicted to form either stem-loop or pseudoknot conformations. As 2A accumulates during EMCV infection, it selectively binds to and stabilises a pseudoknot-like conformation of the PRF stimulatory element, thereby enabling PRF, producing *trans*-frame product 2B* and downregulating the expression of enzymatic viral proteins later in infection. 2A also binds directly to the small ribosomal subunit at the translational GTPase factor binding site, progressively inhibiting both initiation and elongation as it accumulates. This may contribute to the shutdown of host cell translation during lytic infection.

Supplementary Figures

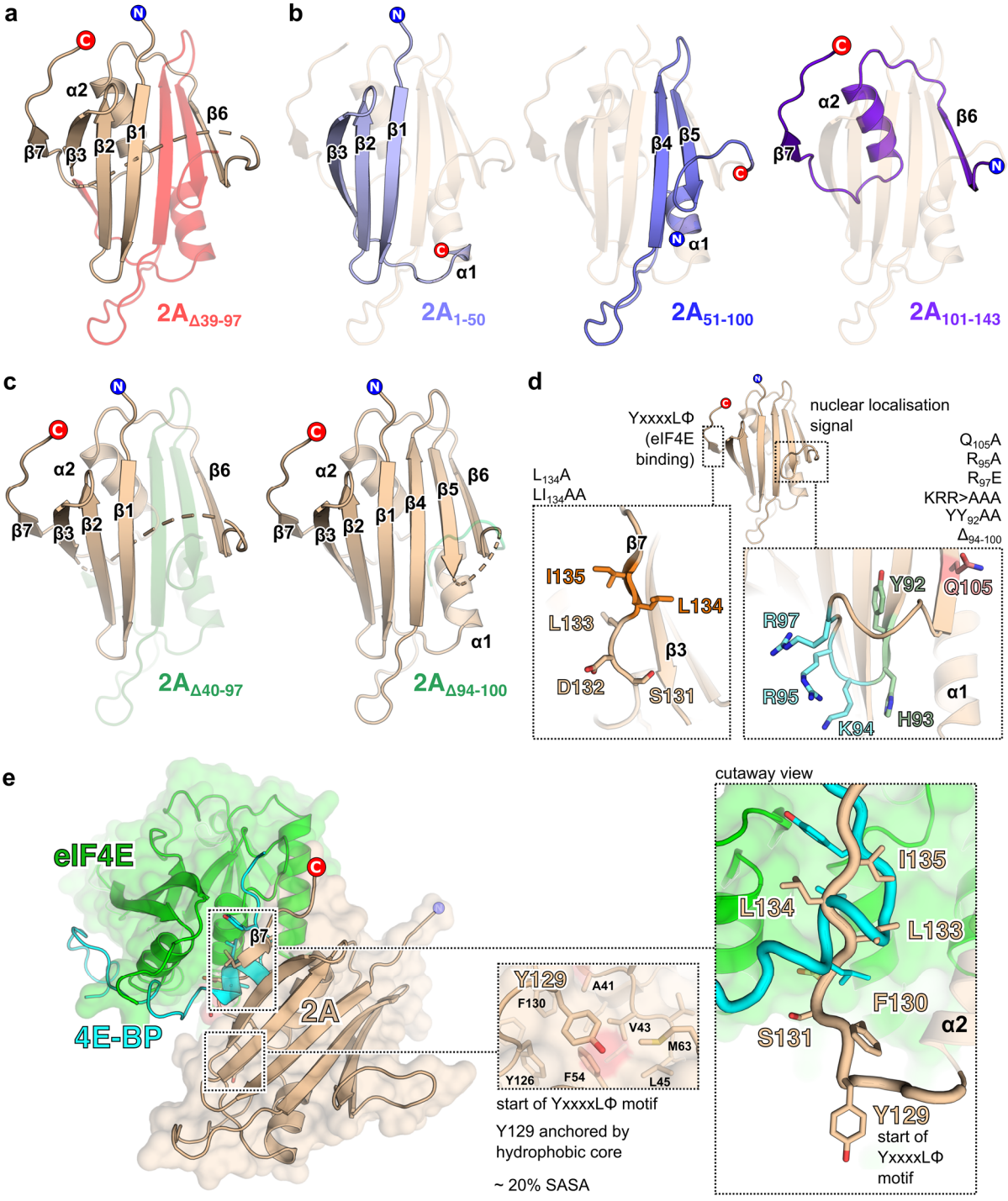

Supplementary Figure 1 – related to **Figure 1. Details of previously described 2A sequence motifs, deletions and point mutations. a,** Structural consequences of the $2A_{\Delta 39\text{-}97}$ mutation described by Svitkin *et al* [1]. Deleted amino acids are highlighted in red. **b,** Truncation fragments $2A_{1\text{-}50}$, $2A_{51\text{-}100}$ and $2A_{101\text{-}143}$ described by Petty *et al* [2]. In each case the remaining fragment is highlighted in blue and overlaid against the structure of the full protein for context. **c,** Deletion mutants $2A_{\Delta 40\text{-}97}$ and $2A_{\Delta 94\text{-}100}$ as described by Groppo *et al* [3]. Deleted

amino acids are highlighted in green. **d,** Location of point-mutations made by Groppo *et al* in the putative nuclear localisation sequence and putative C-terminal YxxxxLΦ eIF4E binding motif. Mutated amino acids are shown as coloured sticks. **e,** Comparison of 4E-BP1 YxxxxLΦ binding motif and the putative YxxxxLΦ motif in 2A. The crystal structure of the complex between eIF4E (green) and 4E-BP1 (blue) is shown (Siddiqui et al., 3U7X) with 2A (wheat) docked via least-squares superposition of the YxxxxLΦ motif. <*Insets*> Contrast between the 2A YxxxxLΦ motif, in an extended β-strand conformation (wheat), and the 4E-BP1 YxxxxLΦ motif, in a compact α-helical conformation, with Y129 partially buried (~ 20% solvent-accessible surface area; SASA). 2A binding to eIF4E is thus not compatible with the known 4E-BP1 interface without substantial conformational rearrangement.

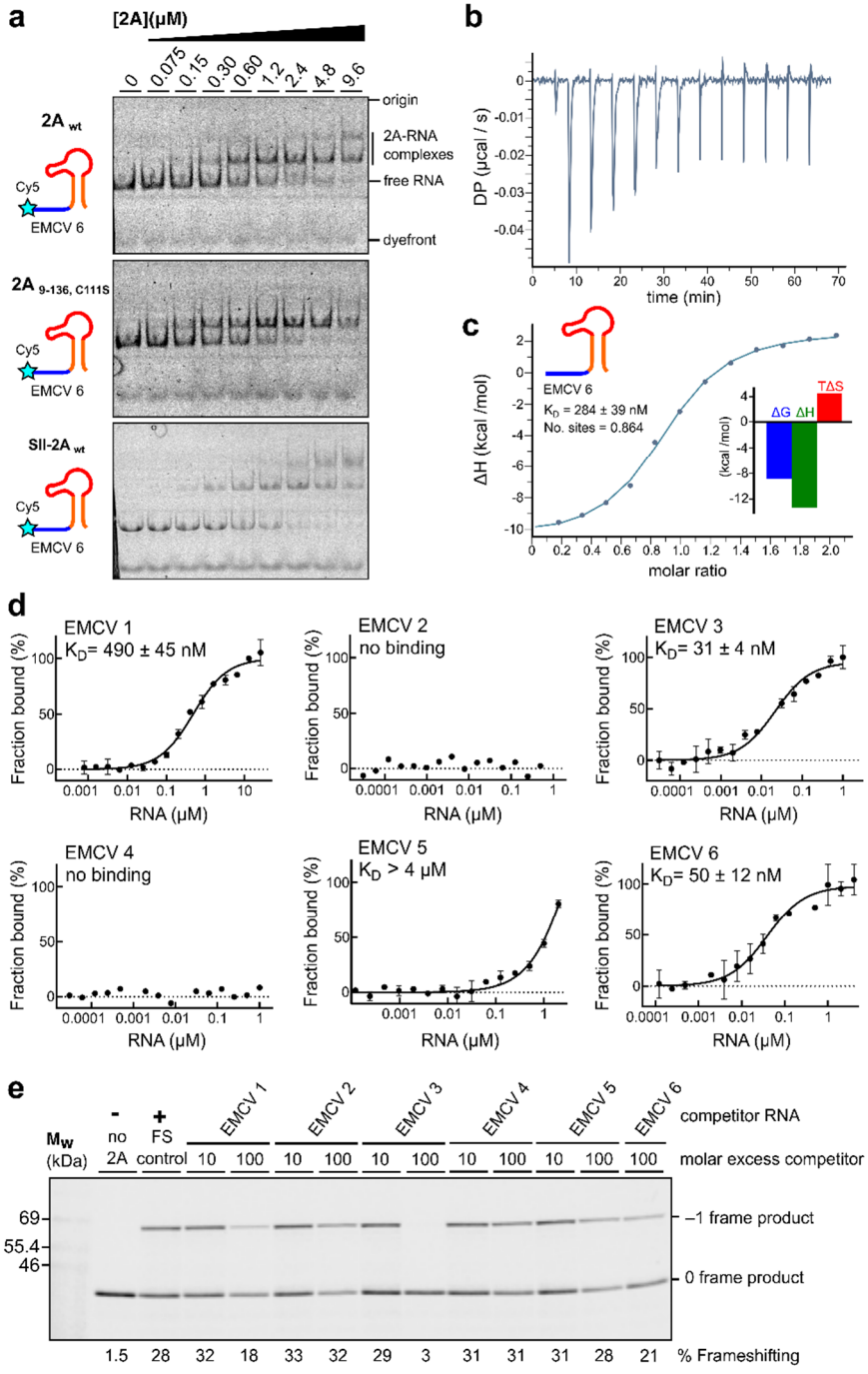

Supplementary Figure 2 – related to **Figure 2. The 2A-RNA interaction does not require disulfide bond formation and is an exergonic process with nanomolar affinity and 1:1 stoichiometry. a,** Side-by-side comparisons of $2A_{wt}$, $2A_{9\text{-}136;\ C111S}$ and SII-$2A_{wt}$. Equivalent RNA binding is observed in all cases by EMSA analyses conducted with 50 nM Cy5-labelled EMCV 6 RNA and 2A concentrations between zero and 9.6 μM. Following non-denaturing electrophoresis, fluorescence was imaged using a Typhoon scanner. Showing representative gels from two independent experiments. **b,** Baseline-corrected differential power (DP) versus time for ITC titration of EMCV 6 RNA into 2A protein. **c,** Normalized binding curve showing integrated changes in enthalpy (ΔH) against molar ratio for titration in **b**, showing a ~1:1 molar

ratio and nanomolar affinity <*Inset*> Histogram showing relative contributions of ΔH and TΔS terms to the overall exergonic interaction. **d,** MST binding curves and reported K_D values of fluorescently labelled 2A protein (5 nM) and short unlabelled RNAs (as in **Fig. 2a, b**) at concentrations between 800 pM – 26 μM for EMCV 1 and 120 pM – 4 μM for EMCV 2–6. All measurements were repeated as two independent experiments and error bars represent the standard deviation from the mean. **e,** Experiment showing the effects of titrating excess short RNAs (EMCV 1–6) as competitors into an *in vitro* frameshift reporter assay. The concentrations of the reporter mRNA and 2A were kept constant in the RRL and short RNAs were added in 10- and 100- fold molar excess relative to the reporter mRNA, as indicated. Translation products were visualised by using ^{35}S-Met autoradiography, and % frameshifting was calculated following densitometry and correction for the number of methionines present in 0 frame and –1 frame products. Showing representative gel from two independent experiments.

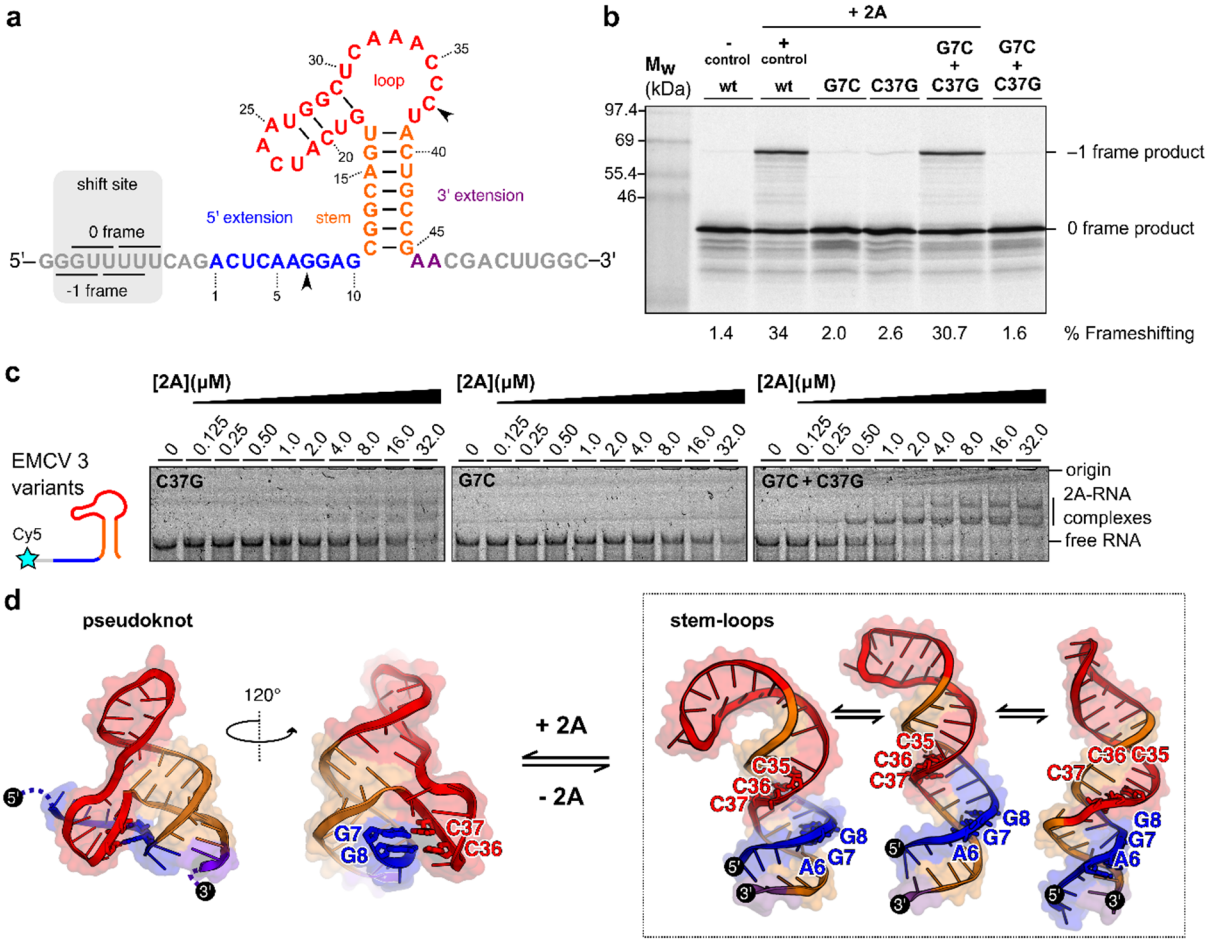

Supplementary Figure 3 – related to **Figure 2 and 3. Mutational analysis of the RNA stimulatory element suggests the existence of a pseudoknot-like conformation. a,** Schematic diagram showing numbered sequence of the EMCV 6 minimal PRF stimulatory element. **b,** Frameshifting assays showing evidence for a base-pairing interaction between G7 and C37. Individual G7C and C37C mutations reduce frameshifting to near-background levels. However, the double mutation (which would permit a compensatory C-G base-pair to form) restores frameshifting to wild-type levels. Representative autoradiogram from two independent experiments **c,** EMSA analyses showing that individual G7C and C37G mutations in the EMCV 6 RNA prevent 2A binding, but the double G7C+C37G mutation restores binding. Experiments were conducted with 50 nM Cy5-labelled EMCV 3 RNA variants and 2A concentrations between zero and 32 μM. Following non-denaturing electrophoresis, fluorescence was imaged using a Typhoon scanner. Showing representative gels from two independent experiments. **d,** Hypothetical equilibrium between several predicted stem-loops and alternate pseudoknot conformations, colour-coded as in **a**. The pseudoknot-like conformation involves base pairs between G7 and G8 in the 5′ extension and C36 and C37 in the loop (shown as sticks). These interactions are not maintained in any predicted stem-loop conformation. Predicted stem loops may involve 35 nt (core) or 49 nt (extended) structured

RNA. The predicted pseudoknot involves 40 nt structured RNA. Also see **Supplementary Table 6.**

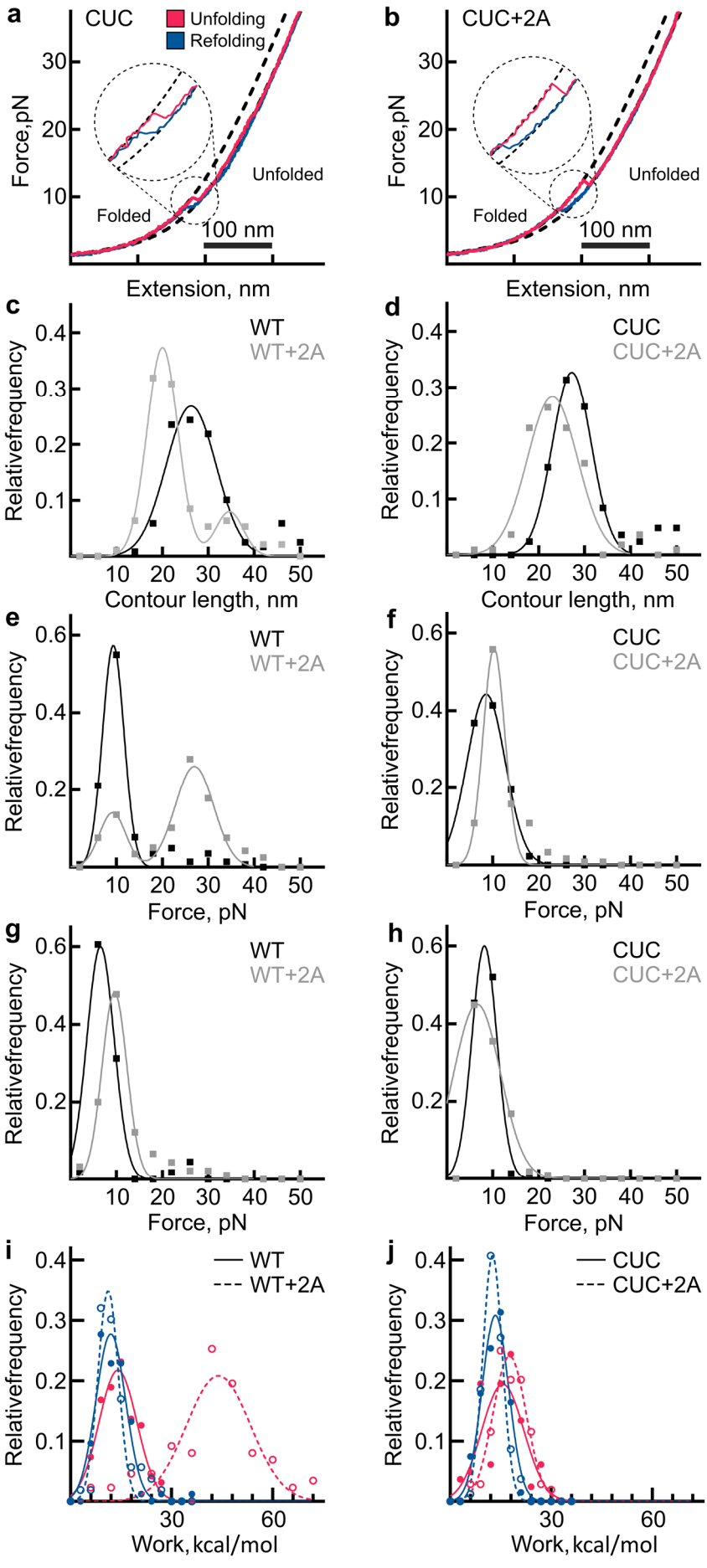
a
CUC
Unfolding
Refolding
Force,pN
Unfolded
Folded
100 nm
Extension, nm
b
CUC+2A
c
WT
WT+2A
Relativefrequency
Contour length, nm
d
CUC
CUC+2A
e
Force, pN
f
g
h
i
WT
WT+2A
Work, kcal/mol
j
CUC
CUC+2A

Supplementary Figure 4 (previous page) – related to **Figure 3. Details of contour length, force and work distributions observed in optical tweezer experiments. a,** Representative force-distance curves of the unfolding (pink) and refolding (blue) transitions of the mutant CUC RNA element (n=85). **b,** Representative force-distance curves of the unfolding (pink) and refolding (blue) transitions of the mutant CUC RNA element in the presence of 300 nM 2A protein (n=109). **c** and **d**, distribution of the contour length changes in the absence (black) and presence (grey) of 2A for WT and CUC RNAs, respectively. Dots represent experimental data points while the line corresponds to the Gaussian fit. **e** and **f**, distribution of the unfolding forces in the absence (black) and presence (grey) of 2A for WT and CUC RNAs, respectively. **g** and **h**, distribution of the refolding forces in the absence (black) and presence (grey) of 2A for WT and CUC RNAs, respectively. **i** and **j**, distribution of unfolding (pink) and refolding (blue) work in the absence (solid) and presence (dashed) of 2A for WT and CUC, respectively.

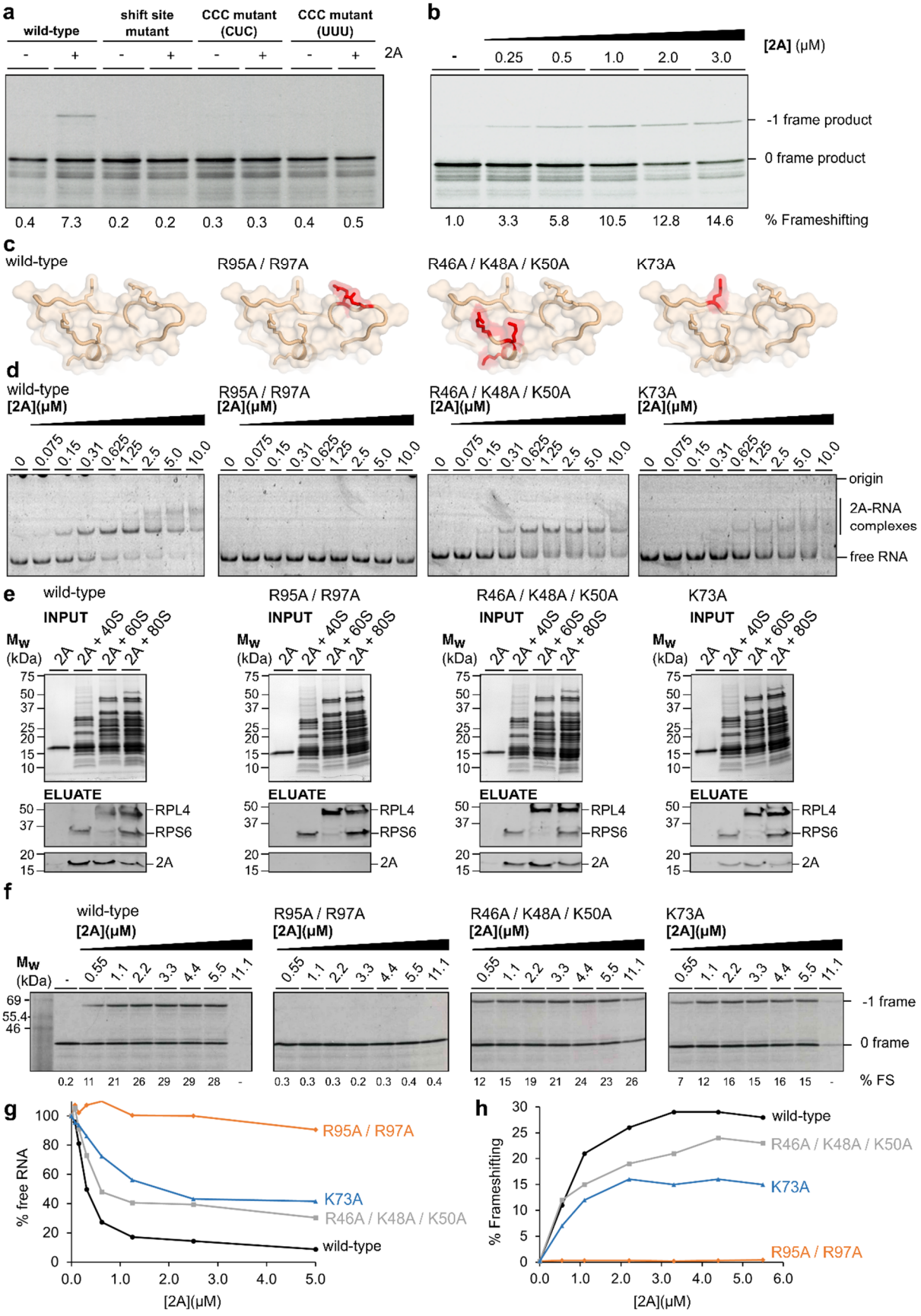

Supplementary Figure 5 – related to **Figures 5 and 6. Mutational analysis of 2A RNA binding residues observed in the 70S$_{IC}$-2A structure. Mutation of the 'arginine loop'**

disrupts binding to both stimulatory element RNA and mammalian ribosome subunits, and inhibits PRF. a, Frameshifting assay showing the reconstitution of 2A-dependent PRF in a prokaryotic *in vitro* translation system. Translation products were visualised by ^{35}S-Met autoradiography and % frameshifting was calculated following densitometry and correction for the number of methionines present in 0 frame and –1 frame products. Representative autoradiograms from two independent experiments. **b,** PRF efficiency in the prokaryotic system is proportional to 2A concentration. At high levels, 2A displays inhibitory effects on total translation. Data analysed as above. **c,** Mutagenesis of residues at the 2A RNA binding surface observed in the $70S_{IC}$-2A structure. The locations of mutations R95A/R97A, R46A/K48A/K50A and K73A are highlighted in red and shown as sticks. **d,** EMSA analyses showing effects of the above mutations on stimulatory element RNA binding, compared to a wild-type control. Panels ordered left-right, as in **a**. Experiments were conducted with 50 nM Cy5-labelled EMCV 6 RNA and 2A concentrations between zero and 10 μM. Following non-denaturing electrophoresis, fluorescence was imaged using a Typhoon scanner. Representative gels from two independent experiments. **e,** Gel-filtration experiments showing effects of the above mutations on eukaryotic ribosome binding, compared to a wild-type control. Panels ordered left-right, as in **a**. Excess 2A (2.5 μM) was incubated with 40S, 60S and 80S ribosomes (0.4 μM) prior to gel filtration chromatography using S200HR spin columns. In these experiments, 2A will only elute if bound to ribosomes. The input <*upper*> was analysed by 4-20% gradient SDS page and visualised by staining with Imperial protein stain. The eluate <*lower*> was analysed by western blot to detect 2A, RPS6 (small ribosomal subunit) and RPL4 (large ribosomal subunit). Experiments were performed once, and all mutant samples were processed at the same time as wild-type. **f,** Frameshift reporter assays showing the effects of the above mutations on *in vitro* translation in RRL. Translation products were visualised by ^{35}S-Met autoradiography and % frameshifting was calculated following densitometry and correction for the number of methionines present in 0 frame and –1 frame products. Representative autoradiograms from two independent experiments. **g,** Plot of % Free RNA vs. 2A concentration, based on densitometric quantification of EMSAs in **b**. **h,** Plot of % Frameshifting vs. 2A concentration, based on quantification reported in **d**.

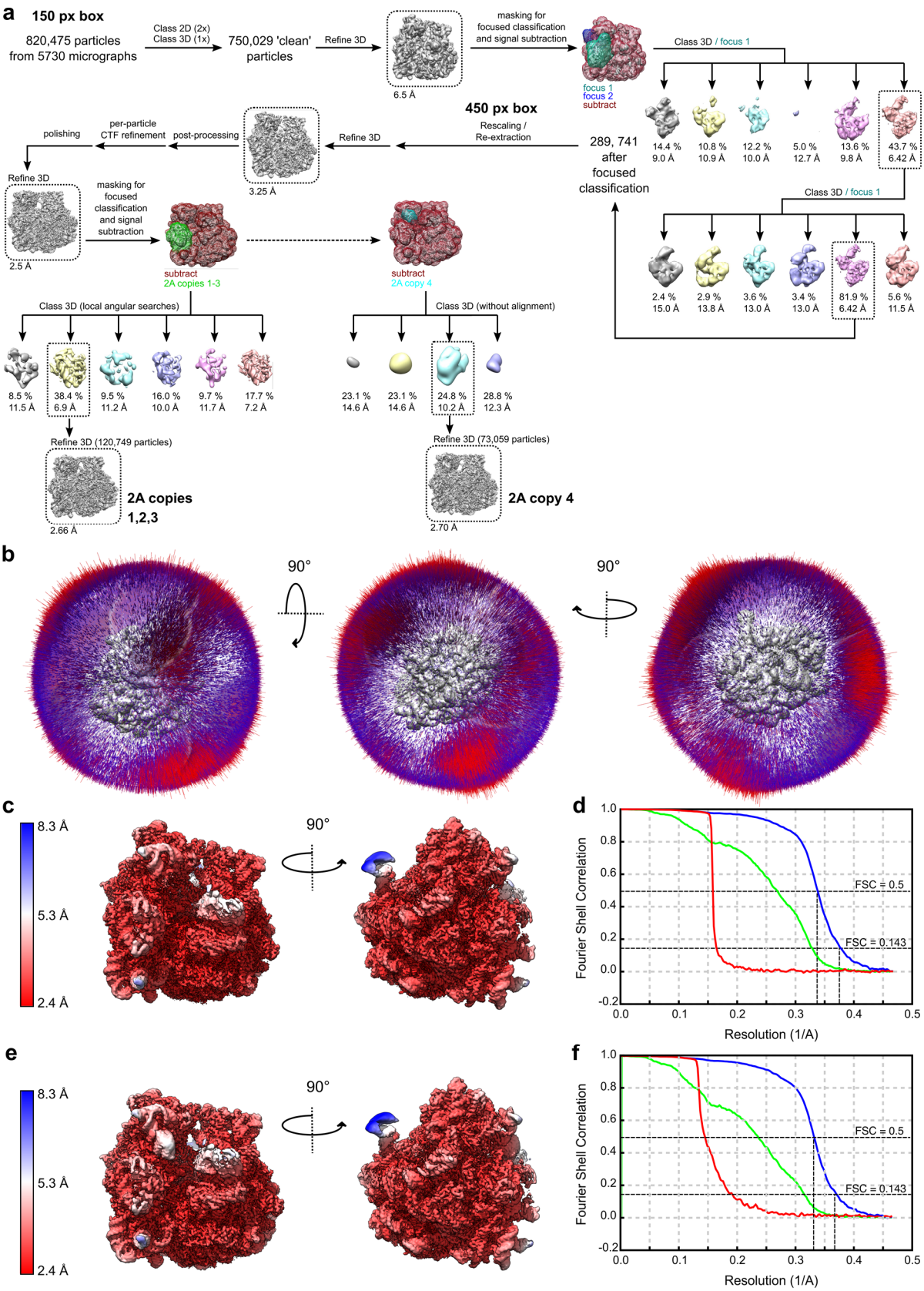

Supplementary Figure 6 – related to **Figures 5, 6 and 7. Details of cryo-EM image processing and map validation. a,** Schematic summary of steps in cryo-EM data processing. **b,** Three orthogonal views showing the angular distribution of particles contributing to the final

3D reconstruction. This is shown for the highest-resolution Refine3D result i.e. immediately after particle polishing. **c,** Local-resolution map for the final reconstruction of 70S-2A_3. The surface is coloured by local resolution from red (highest; 2.4 Å) to blue (lowest; 8.3 Å). **d,** Gold-standard Fourier shell correlation (FSC) curve for the 70S-2A_3 map. Masked (blue), unmasked (green) and phase-randomised masked (red) plots are shown. **e,** Local-resolution map for the final reconstruction of 70S-2A_4, details as in **c**. Local resolution estimate for 2A4 is ~ 5 – 7 Å. **f,** Gold-standard Fourier shell correlation (FSC) curve for the 70S-2A_4 map. Details as in **d**.

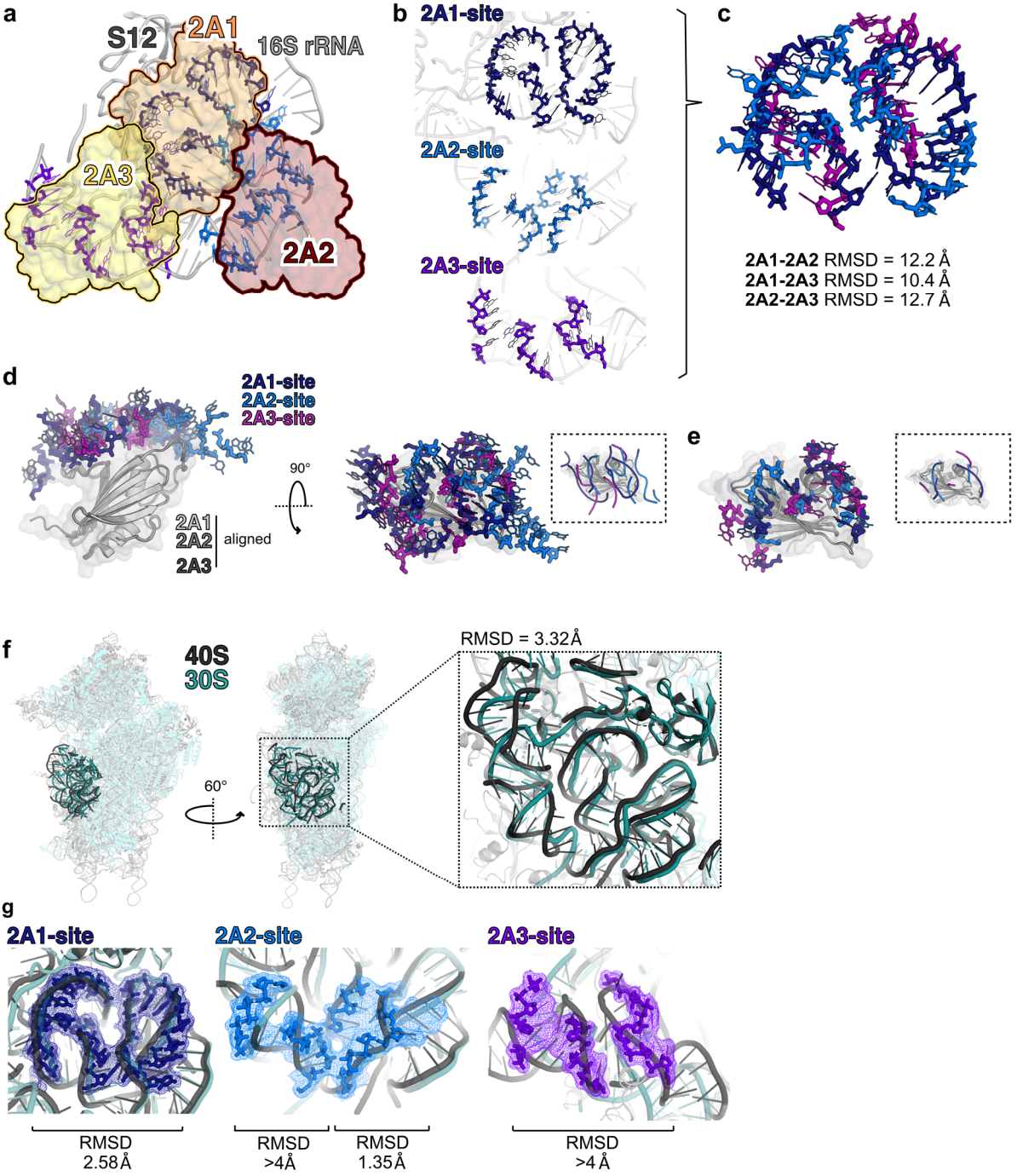

Supplementary Figure 7 – related to **Figure 5 and 6. Analysis of 2A binding sites observed on *E. coli* 16S rRNA. The 2A1 site is the most structurally conserved. a,** Diagram showing the binding sites of each 2A molecule (coloured sticks) on the 16S rRNA (grey cartoon). Binding sites were defined as rRNA residues within 8.0 Å distance of each 2A molecule, as determined by a PDBePISA analysis of molecular contacts. **b,** As above, showing each of the 2A binding sites separately (sticks), superimposed on local 16S rRNA (grey cartoon). **c,** Backbone superposition of the three sites fails to reveal a common binding motif. **d,** Superposition of binding sites (sticks) based on first aligning the three 2A molecules (grey ribbon diagrams). Two orthogonal views are shown. <*Inset*> cartoon representation of

RNA backbone shown in the top-down view. **e,** As in **d**, but trimmed to show spatial conservation (i.e. only residues within 3.0 Å of those in other binding sites. **f,** Structural superposition of 2A binding sites observed on *E. coli* 16S rRNA (30S, turquoise) with equivalent sites on *O. cuniculus* 18S rRNA (40S, black) The 30S 2A binding patch and equivalent 40S rRNA (black) are highlighted. <*Inset*> Close-up view of 2A binding sites after backbone superposition. **g,** Local alignment of each individual 2A binding site to nearest equivalent in 40S rRNA (black). Per site, deviation from the starting position in the 30S rRNA (green) was permitted. The binding site for 2A1 is the most structurally conserved between 30S and 40S.

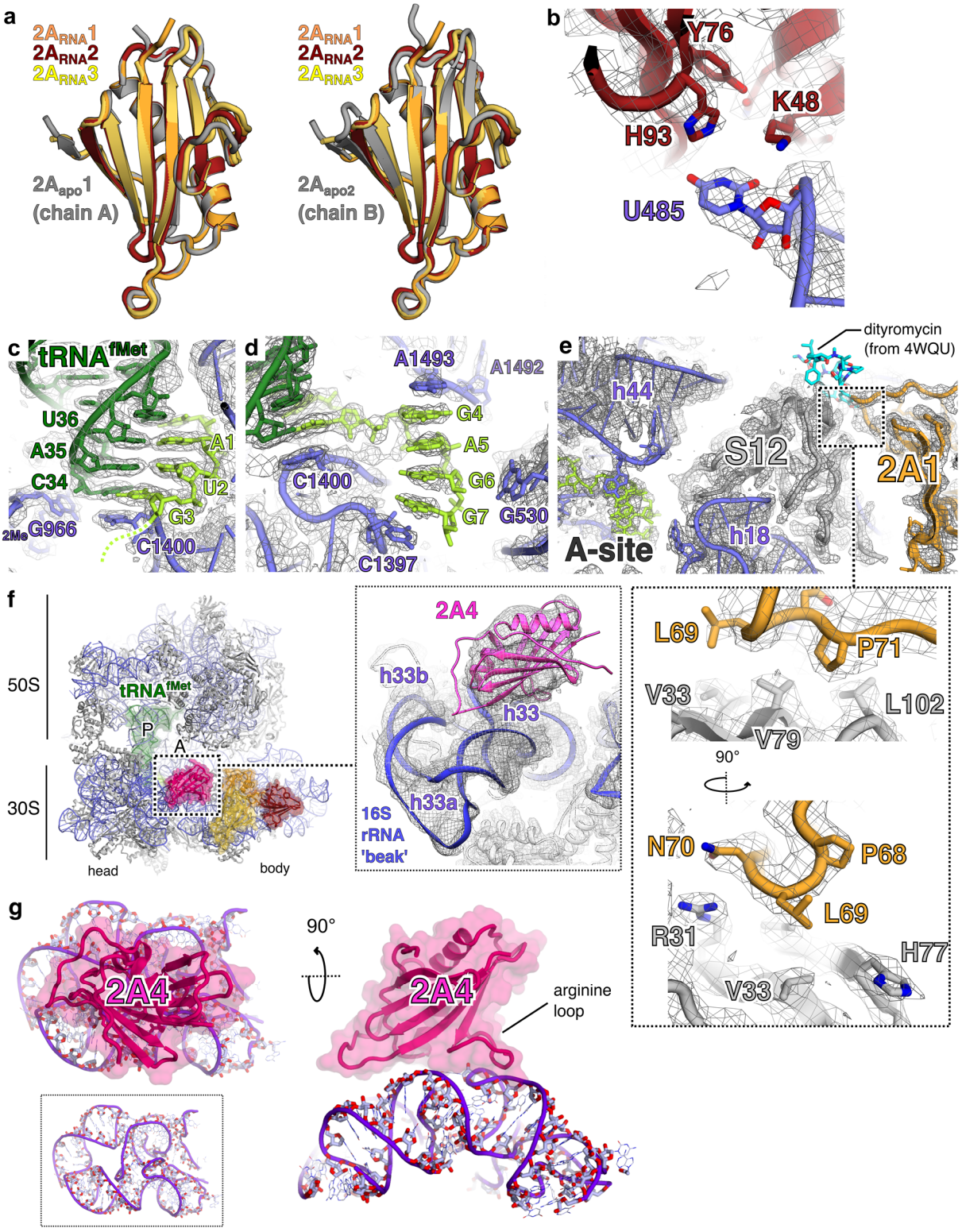

Supplementary Figure 8 – related to **Figure 5, 6 and 7. Structural details of the 70S decoding centre, 2A1 interaction with S12 and 2A4 binding site. a,** Comparison between conformations of 2A protein in RNA bound states (orange, red, yellow) and the two unliganded states observed by NCS in the crystal structure. The $2A_{apo}1$ conformation observed in chain A is most similar to the RNA-bound state. Structural alignments were performed by least-

squares superposition of the C_α backbone. **b,** Details of a base-specific interaction between U485 (helix 17 of 16S) and a pocket on the surface of 2A2 (red). **c,** Cryo-EM density at the P-site. Codon-anticodon pairing between the mRNA (lime) and the initiator $tRNA^{fMet}$ (dark green). The tRNA is in an undistorted P/P conformation as expected. **d,** Cryo-EM density at the A-site, coloured as in **b**. Additional 30S residues with roles in decoding are shown as sticks (purple). **e,** Details of a hydrophobic 2A1 interaction with ribosomal protein S12. The contact surface is on the factor-binding face of S12, away from the decoding centre. The binding site of antibiotic dityromycin on S12 (from 4WQU[4] [http://doi.org/10.2210/pdb4wqu/pdb]) is shown with blue sticks. **f,** Ribbon diagram of initiated 70S-mRNA-$tRNA^{fMet}$-2A complex showing the location of the fourth copy of 2A (pink) present in a smaller population of particles. Ribosome sites are labelled A and P. The initiator $tRNA^{fMet}$ (dark green), mRNA (lime), 2A1 (orange), 2A2 (red) and 2A3 (yellow) are also shown. <*Inset*> Section of the 70S-$2A_4$ local resolution map showing electron density at the 2A4 binding site. 2A4 binds to the 3′ major 'beak' domain of the 16S rRNA present in the 30S 'head', via electrostatic interactions with the ribose phosphate backbone of helices 33 and 34. **g,** Details of 2A4 interaction with 16S rRNA (purple) in two orthogonal views.

Additional Data [http://dx.doi.org/10.17632/gkpwngy65h.2] – related to **Figures 2 and 4.**
Capillary scans and thermophoretic time-traces of microscale thermophoresis (MST) measurements of binding between 2A and RNA. a, EMCV RNA 1, **b,** EMCV RNA 2, **c,** EMCV RNA 3, **d,** EMCV RNA 4, **e,** EMCV RNA 5, **f,** EMCV RNA 5, **g,** EMCV RNA 6, **h,** 30S, **i,** 50S, **j,** 40S, **k,** 60S, **l,** 70S and **m,** 70S IC. The protein was fluorescently labelled, while unlabelled ligands were added at different concentrations. The grey boxes in the capillary scans mark 20% above and below the average peak fluorescence, the acceptable limit of deviations across the fluorescence scans. Blue and red boxes in the time-course traces represent the temperature jump and MST-on time (10s), respectively. In all cases, there is no adsorption of the labelled protein to the capillaries. See Fig. 2 and Fig. 4 for the resulting binding curves.

Supplementary Tables

Supplementary Table 1 – Crystallographic data collection and refinement. Related to **Figure 1.**

	Native (PDB 7BNY)	SeMet derivative		
Data collection				
Space group	$P6_222$			
Cell dimensions				
a, *b*, *c* (Å)	91.5, 91.5, 316.5			
α, β, γ (°)	90.0, 90.0, 120.0			
		Peak	*Inflection*	*Remote (High E)*
Wavelength (Å)	0.97958	0.97965	0.97974	0.97635
Resolution (Å)	43.91–2.62 (2.67–2.62)	76.53–2.91 (2.96–2.91)	79.36–3.08 (3.13–3.08)	79.0–2.98 (3.03–2.98)
R_{pim}	0.053 (0.640)	0.062 (0.521)	0.067 (0.548)	0.048 (0.473)
$I / \sigma I$	11.5 (1.0)	9.9 (1.2)	9.3 (1.1)	12.9 (1.2)
Completeness (%)	100.0 (99.8)	99.7 (99.2)	99.9 (99.6)	99.6 (99.0)
Anomalous	-	99.2 (98.8)	99.3 (99.2)	99.1 (98.7)
Redundancy	18.9 (19.4)	18.6 (17.2)	18.6 (19.8)	37.4 (38.5)
Anomalous	-	10.4 (9.3)	10.5 (10.7)	21.0 (20.9)
$CC_{1/2}$	0.998 (0.728)	0.997 (0.804)	0.997 (0.822)	0.999 (0.834)
CC_{anom}	-	0.400 (0.024)	0.167 (0.000)	0.314 (0.002)
Refinement				
Resolution (Å)	43.91–2.62 (2.71–2.62)			
No. reflections	24589 (2375)			
R_{work} / R_{free}	0.2254 / 0.2511			
No. atoms				
Protein	4404			
Ligand/ion	45			
Water	147			
B-factors				
Protein	75.0			
Ligand/ion	110.0			
Water	64.9			
R.m.s deviations				
Bond lengths (Å)	0.003			
Bond angles (°)	0.741			

*Data were recorded from a single native crystal and a single crystal of selenomethionine-derivatised protein (SeMet). *Values in parentheses are for the highest-resolution shell.

Supplementary Table 2 - Summary of dissociation constants (K_D) measured by microscale thermophoresis with various 2A interaction partners. Related to **Figures 2, 4 and Supplementary Figure 2.**

	K_D (LABELLED 2A)	K_D (LABELLED RNA)
EMCV 1	360 ± 34 nM	490 ± 45 nM
EMCV 2	No binding	No binding
EMCV 3	40 ± 2 nM	31 ± 4 nM
EMCV 4	No binding	No binding
EMCV 5	> 4 µM (does not reach saturation)	> 4 µM (does not reach saturation)
EMCV 6	70 ± 14 nM	50 ± 12 nM
40S	10 ± 2 nM (apparent)	N/A
60S	> 1000 nM (apparent; does not reach saturation)	N/A
30S	4 ± 1 nM (apparent)	N/A
50S	> 500 nM (apparent)	N/A
70S	49 ± 13 nM (apparent)	N/A
70S IC	> 60 nM (apparent; does not reach saturation)	N/A

Supplementary Table 3 – Summary of experimental OT results and predicted mfold data for EMCV WT and CUC RNAs in the absence or presence of 2A. Results were determined by gaussian fitting of the distribution histograms of obtained data (number of tethers used in the experiments was >15, and number of force trajectories range between 85-120). Related to **Figure 3 and Supplementary Figure 4.** Uncertainties represent standard deviations.

	WT	WT + 2A	CUC	CUC + 2A
Contour length change, nm	26.3±5.4	20.1±3.4	27.2±4.3	23.0±5.5
Unfolding force, pN	9.3±2.3	9.2±2.9 27.0±4.2	8.6±4.2	10.3±2.4
Refolding force, pN	6.5±3.0	9.6±2.7	8.2±2.7	6.6±5.1
Gibbs free energy (mfold), kcal/mol	-14.0±0.7 (SL), -16.2±0.8 (extended SL)		-14.0±0.7 (SL), -16.2±0.8 (extended SL)	
Gibbs free energy (experiment), kcal/mol	-13.6±4.6* -11.6±0.9**	- -26.5±8.7**	-14.5±4.7* -11.0±1.6**	-15.5±5.0* -12.9±1.2**

*Calculated by applying Crook's fluctuation theorem to unfolding/refolding work distributions. Uncertainty represents standard deviation.

**Calculated by applying Jarzynski's equality. Uncertainty represents root of mean square error.

Of note, free energy values of the CUC and WT (without 2A) RNAs were in good agreement regardless of the calculation method employed.

Supplementary Table 4 – Cryo-EM data collection, processing, refinement and validation. Related to **Figures 5–7, Supplementary Figure 6 and 7**.

	70SIC-2A complex (EMDB-12635) (PDB 7NWT)
Data collection and processing	
Magnification	75,000x
Voltage (kV)	300
Electron exposure (e–/Å^2)	54.4
Defocus range (μm)	–1.2, –1.5, –1.8, –2.1, –2.4, –2.7, –3.0
Pixel size (Å)	1.07
Symmetry imposed	C1
Initial particle images (no.)	820,475
Final particle images (no.)	120,749
Map resolution (Å)	2.66
FSC threshold	0.143
Map resolution range (Å)	2.66 – 8.3
Refinement	
Initial model used (PDB code)	5MDZ
Model resolution (Å)	2.66
FSC threshold	0.143
Map sharpening *B* factor (Å^2)	-88.5
Model composition	
Non-hydrogen atoms	149932
Protein residues	6355
Nucleic acid residues	4641
Ligands	439
B factors (Å^2)	
Protein	53.87
Nucleic Acid	49.01
Ligand	34.31
R.m.s. deviations	
Bond lengths (Å)	0.011
Bond angles (°)	0.830
Validation	1.73
MolProbity score	4.84
Clashscore	2.95
Poor rotamers (%)	
Ramachandran plot	
Favored (%)	97.41
Allowed (%)	2.58
Disallowed (%)	0.02

Supplementary Table 5 – Oligonucleotide sequences. Related to **Methods**.

RNAs	SOURCE / REF
EMCV 1 used in EMSA and MST assays: 5' – ACUCAAGGAGCGGCAGUGUCAUCAAUGGCUCAAACCCUACUGCCGAAC GACUUG – 3'	Integrated DNA Technologies (IDT)
EMCV 2 used in EMSA and MST assays: 5' – AGCGGCAGUGUCAUCAAUGGCUCAAACCCUACUGCCGAACGACUUG – 3'	Integrated DNA Technologies (IDT)
EMCV 3 used in EMSA and MST assays: 5' – GGGUUUUUCAGACUCAAGGAGCGGCAGUGUCAUCAAUGGCUCAAACCC UACUGCCGAA – 3'	Integrated DNA Technologies (IDT)
EMCV 3a used in EMSA 5' – GGGUUUUUCAGACUCAAGGAGCGGCAGUGUCAUCAAUGGCUCAAACC GUACUGCCGAA – 3'	Integrated DNA Technologies (IDT)
EMCV 3b used in EMSA 5' – GGGUUUUUCAGACUCAACGAGCGGCAGUGUCAUCAAUGGCUCAAACCC UACUGCCGAA – 3'	Integrated DNA Technologies (IDT)
EMCV 3c used in EMSA 5' – GGGUUUUUCAGACUCAACGAGCGGCAGUGUCAUCAAUGGCUCAAACCG UACUGCCGAA – 3'	Integrated DNA Technologies (IDT)
EMCV 4 used in EMSA and MST assays: 5' – AGCGGCAGUGUCAUCAAUGGCUCAAACCCUACUGCCGAA – 3'	Integrated DNA Technologies (IDT)
EMCV 5 used in EMSA and MST assays: 5' – GGGUUUUUCAGACUCAAGGAGCGGCAGUCAAACCCUACUGCCGAACGA CUUG – 3'	Integrated DNA Technologies (IDT)
EMCV 6 used in EMSA and MST assays: 5' – ACUCAAGGAGCGGCAGUGUCAUCAAUGGCUCAAACCCUACUGCCGAA – 3'	Integrated DNA Technologies (IDT)
70S_IC transcribed mRNA (used in 70S IC preparation): 5' – GGGAAUUCAAAAAUUGUUAAGAAUUAAGGAGAUAUACAUAUGGAGGUU UUUAUCACUCAAGGAGCGGCAGUGUCAUCAAUGGCUCAAACCCUACUG CCGAACGACUUGGCCAGATCT – 3'	This work
EMCV CCC OT ssRNA region of the OT construct (used in OT experiments): 5'– GAGGUUUUUAUCCUCAAGGAGCGGCAGUGUCAUCAAUGGCUCAAACCC UACUGCCGAACGACUUGGACUUAAUUUAAAAAAAAAAAAAAAAAA – 3'	This work

EMCV CUC OT ssRNA region of the OT construct (used in OT experiments): 5' – GAGGUUUUUAUCCUCAAGGAGCGGCAGUGUCAUCAAUGGCUCAAACUC UACUGCCGAACGACUUGGACUUAAUUUAAAAAAAAAAAAAAAAAA – 3'	This work

DNA Oligonucleotides	**SOURCE / REF**
E2A_F1 primer (used for cloning EMCV 2A): 5' – AATTCATATGAGCCCCAACCCTTTGGATGTC – 3'	Sigma-Aldrich VC00021
E2A_R1 primer (used for cloning EMCV 2A): 5' – AATTGGATCCCCCGGGATTGGTCTCGACATC – 3'	Sigma-Aldrich VC00021
E2A_F2 primer (used to clone EMCV 2A 9-136 construct): 5' – AATTCATATGAAAACTTACCCAACTCTGCACAT – 3'	Sigma-Aldrich VC00021
E2A_R2 primer (used to clone EMCV 2A 9-136 construct]): 5' – AATTGGATCCTCATTAGTGGATCAAAAGATCTGAAAAGTATCCT – 3'	Sigma-Aldrich VC00021
E2A_mut_F1 mutagenesis primer (used to introduce 2A mutant C111S): 5' – AAAGAGTGGAGGACTTCTGAAGAGAATGTTTTT – 3'	Sigma-Aldrich VC00021
E2A_mut_R1 mutagenesis primer (used to create 2A C111S): 5' – AAAAACATTCTCTTCAGAAGTCCTCCACTCTTT – 3'	Sigma-Aldrich VC00021
E2A_mut_F2 mutagenesis primer (used to create 2A R46A/K48A/K50A): 5' – AACACATGCAGAAGTGGTGCTTGCGTCAGCGACAGCACAAATCAGCTTC CTGAGCAA – 3'	Sigma-Aldrich VC00021
E2A_mut_R2 mutagenesis primer (used to create 2A R46A/K48A/K50A): 5' – TTGCTCAGGAAGCTGATTTGTGCTGTCGCTGACGCAAGCACCACTTCTG CATGTGTT – 3'	Sigma-Aldrich VC00021
E2A_mut_F3 mutagenesis primer (used to create 2A K74A): 5' – CACCGTTAAACCCCTGGGCGAGCACATATCAGGCAGT – 3'	Sigma-Aldrich VC00021
E2A_mut_R3 mutagenesis primer (used to create 2A K74A): 5' – ACTGCCTGATATGTGCTCGCCCAGGGGTTTAACGGTG – 3'	Sigma-Aldrich VC00021
SII_F cloning oligonucleotide (used to insert StrepII-tag into 2A_pGEX6P1): 5' – GATCCTGGTCACATCCGCAGTTTGAAAAAGGTAGCGCAGGTAGTGCAGC AGGTAGCGGTGCAGGTTGGAGCCACCCTCAGTTTGAGAAAG – 3'	Sigma-Aldrich VC00021
SII_R cloning oligonucleotide (used to insert StrepII-tag into 2A_pGEX6P1): 5' – GATCCTTTCTCAAACTGAGGGTGGCTCCAACCTGCACCGCTACCTGCTG CACTACCTGCGCTACCTTTTTCAAACTGCGGATGTGACCAG – 3'	Sigma-Aldrich VC00021
pdluc/EMCV reporter construct sequence (used in frameshift assays): 5'- AAGACAACGGCCGGTTTTTCAGACTCAAGGAGCGGCAGTGTCATCAATG GCTCAAACCCTACTGCCGAACGACTTGGCCAGCAAAcgTATGGGATCAGC CTTTAC– 3'	Napthine et al., 2017
Transcription template forward primer (used in 70S IC preparation): 5' – GTTGTGTGGAATTGTGAGCGGAT– 3'	Microsynth
Transcription template reverse primer (used in 70S IC preparation):	Microsynth

5’ – GGCCAAGTCGTTCGG – 3’	
5' handle T7 forward PCR primer (used to generate OT 5’ handle): 5’ – CTTAATACGACTCACTATAGGTCCTTTCTGTGGACGCC – 3’	Microsynth
5’ handle reverse PCR primer (used to generate OT 5’ handle and clone short ssRNA control construct): 5’ – CATAAATACCTCTTTACTAATATATATACCTTCGTAAGCTAGCGT – 3’	Microsynth
5’ handle short single stranded control PCR primer (used to generate OT 5’ handle for short ssRNA control and clone no ssRNA control construct): 5’- GTAGCTGTCGAGCTCCTGCGAAGAGCGCAACCATGTTATCCAGTGAG– 3’	Microsynth
3’ handle forward PCR primer (used to generate OT 3’ handle and to clone both of the control constructs): 5’ – ATCCTGCAACCTGCTCTTCGCCAG – 3’	Microsynth
3’ handle reverse 5’labeled with **digoxigenin** PCR primer (used to generate OT 3’ handle): 5’ –[Dig]-GTCAAAGTGCGCCCCGTTATCC – 3’	Microsynth
CUC mutant forward cloning oligonucleotide (used to insert the point mutation of CCC motif): 5’ – CTCTACTGCCGAACGACTTGGCC – 3’	Microsynth
CUC mutant reverse cloning oligonucleotide (used to insert the point mutation of CCC motif): 5’ – TTTGAGCCATTGATGACACTGCCG – 3’	Microsynth

The name of each oligonucleotide is highlighted in bold italics, as referred to in **Methods**.

Supplementary Table 6 – Predicted secondary structures of the EMCV PRF RNA element. Related to **Fig. 3** and Supplementary **Fig. 4**.

Structure	Expected contour length, nm / nt	Predicted secondary structure
Primary sequence	55.5 / 94	GAGGUUUUUAUCCUCAAGGAGCGGCAGUGUCAUCAAUGG CUCAAACCCUACUGCCGAACGACUUGGACUUAAUUUAAAA AAAAAAAAAAAAAA
Stem-loop	20.7 / 35	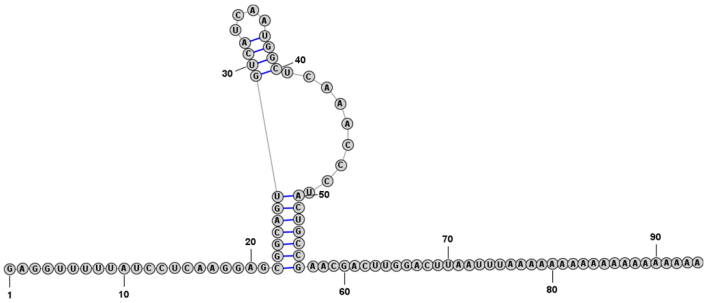
Extended stem-loop	28.9 / 49	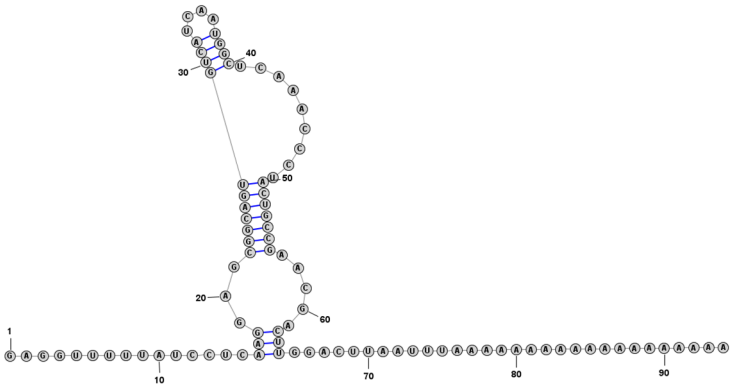
Pseudoknot	23.5 / 40	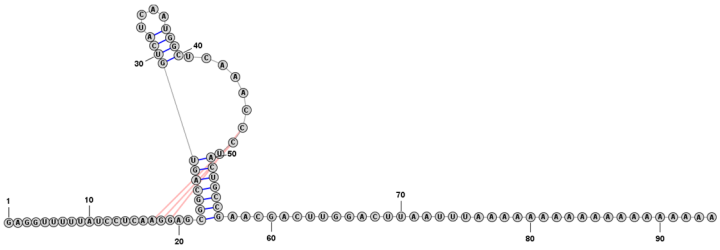

Source Data for Supplementary Figures (uncropped images, autoradiograms, gel scans, phosphorimager scans)

Supplementary Figure 2 – panel A (fluorescent gels)

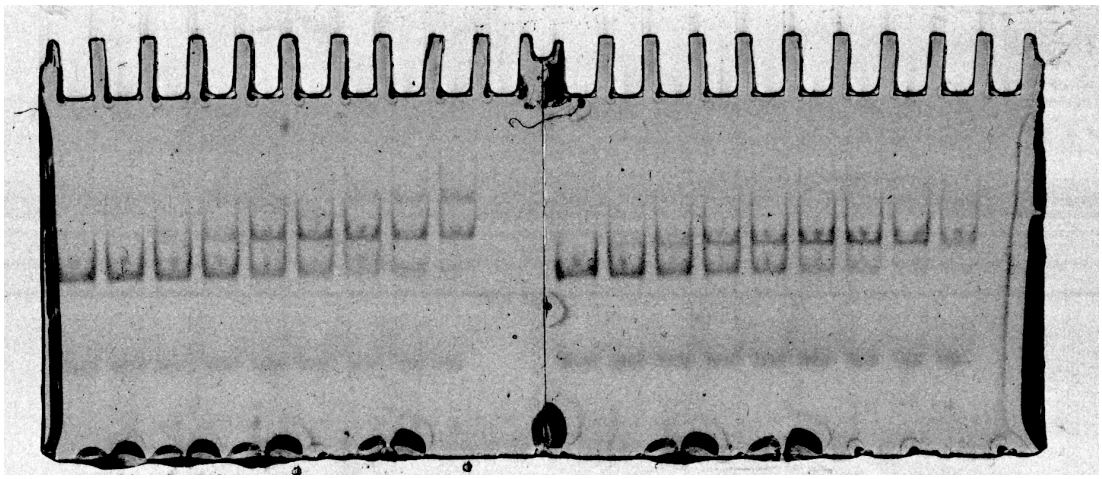

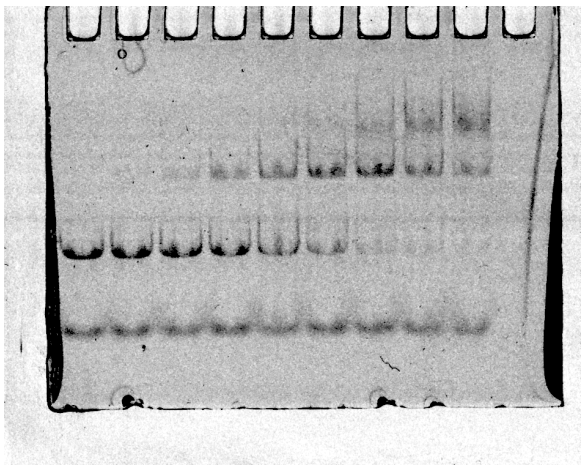

Supplementary Figure 2 – panel E (phosphorimager scan)

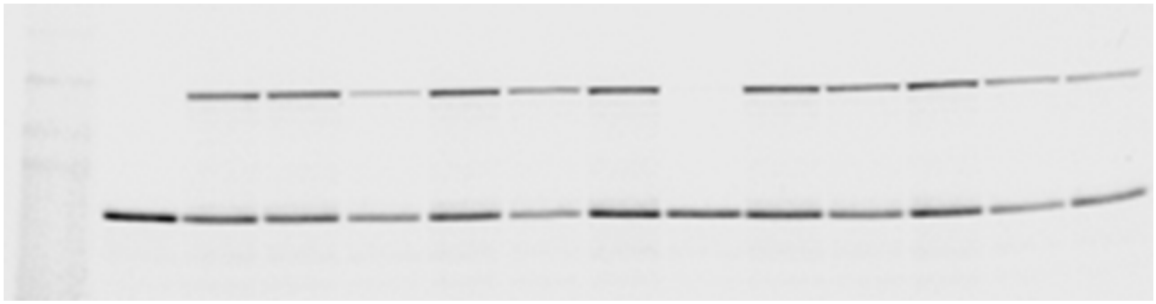

Supplementary Figure 3 – panel B (phosphorimager scan)

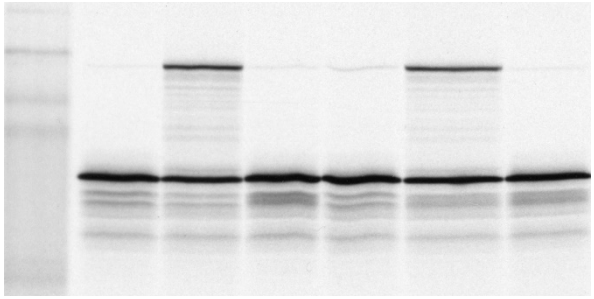

Supplementary Figure 3 – panel C (fluorescent gels)

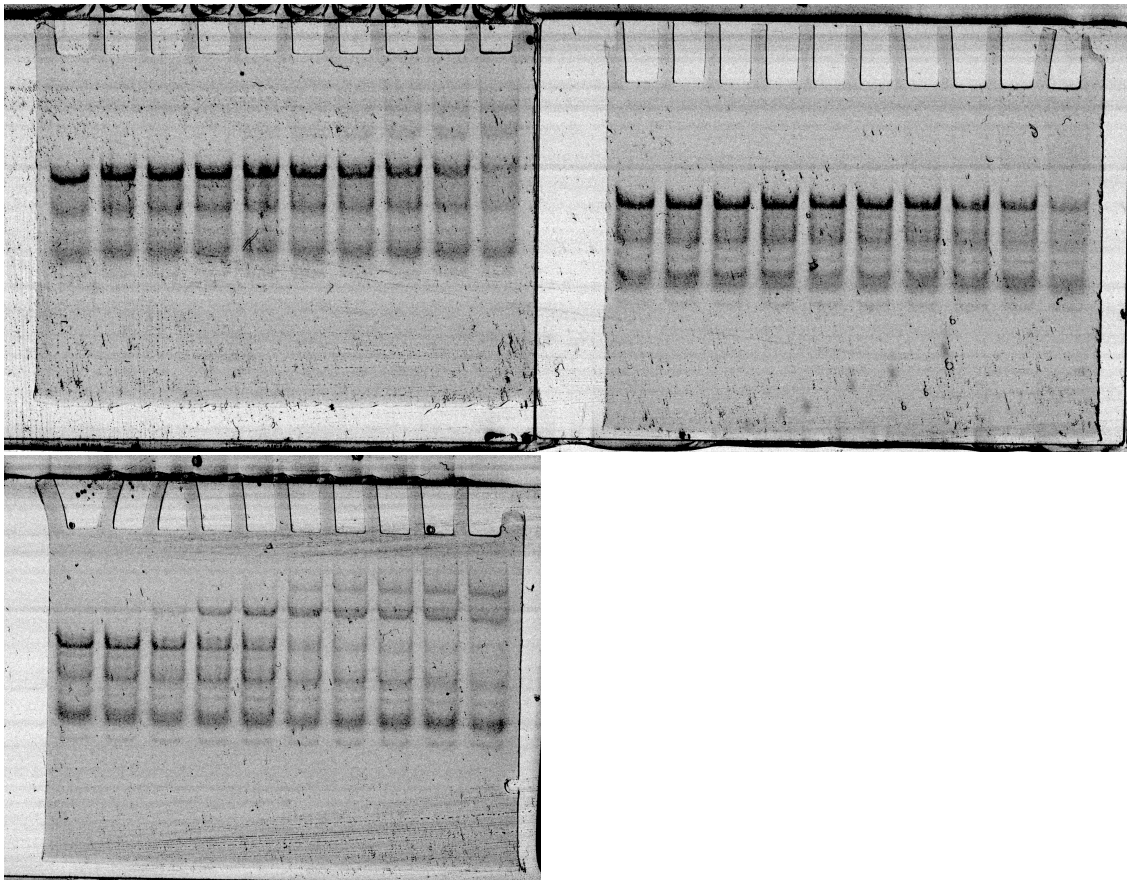

Supplementary Figure 5 – panel A (phosphorimager scan)

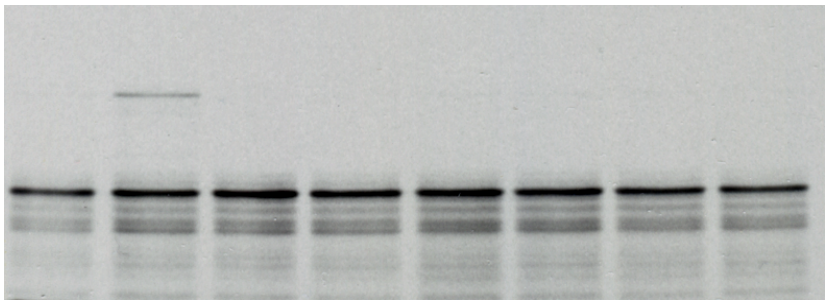

Supplementary Figure 5 – panel B (phosphorimager scan)

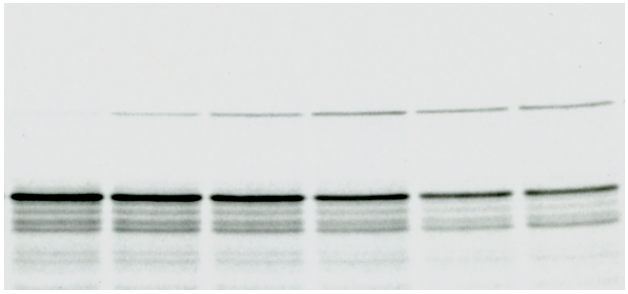

Supplementary Figure 5 – panel D (fluorescent gels)

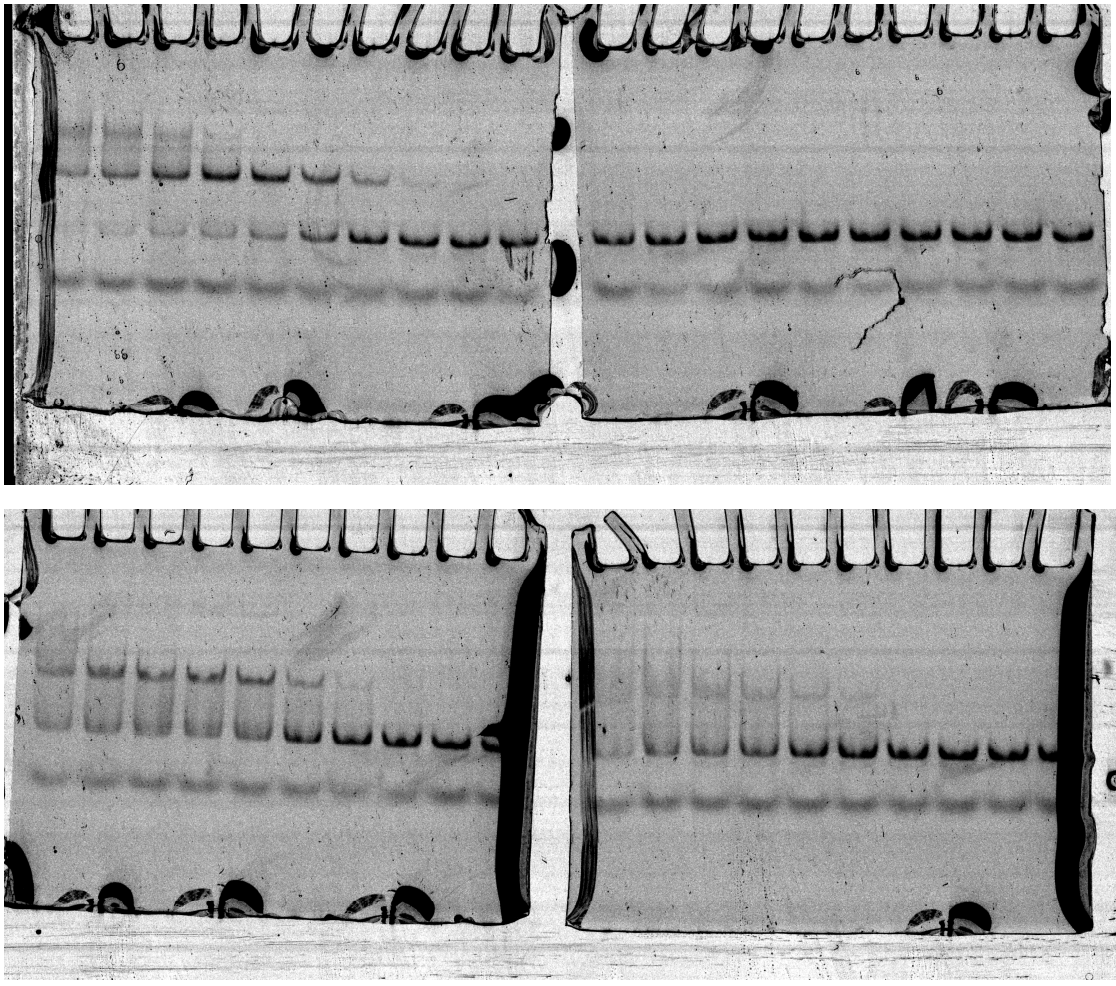

Supplementary Figure 5 – panel E (Imperial-stained input gels. The molecular weight ladders are the Precision Plus Protein Dual Color Standards [BioRad, 1610374])

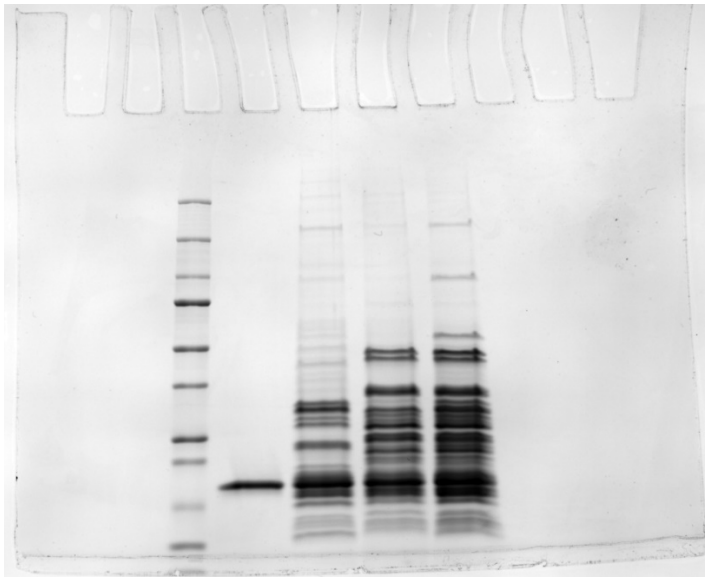

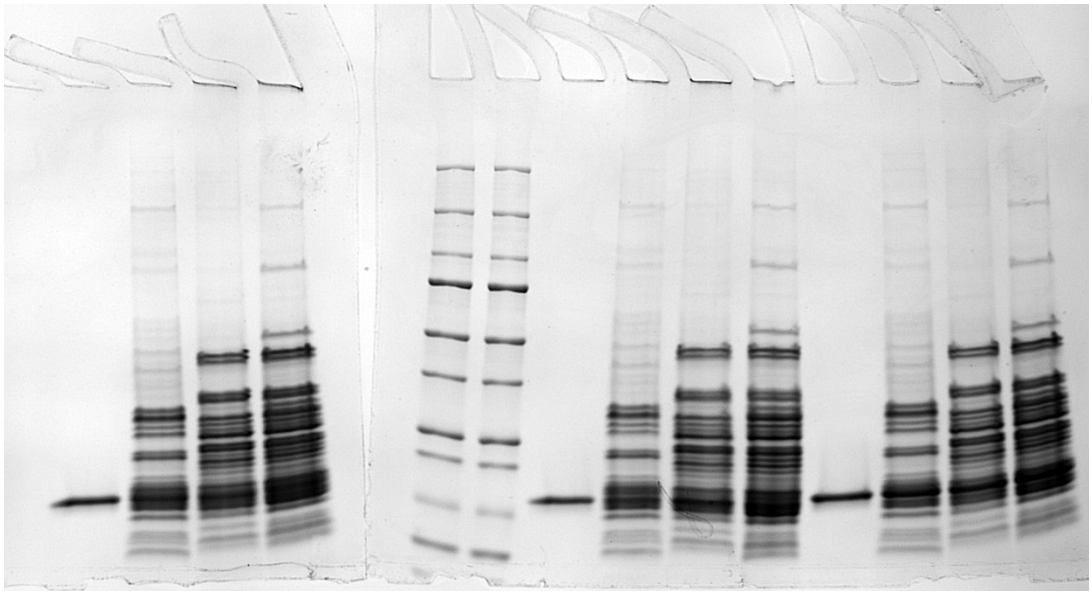

Supplementary Figure 5 – panel E (LI-COR fluorescent scans of eluate blots, green channel – anti-S6 and anti-L4 ribosomal proteins; red channel anti-2A. The molecular weight ladders are the Precision Plus Protein Dual Color Standards [BioRad, 1610374])

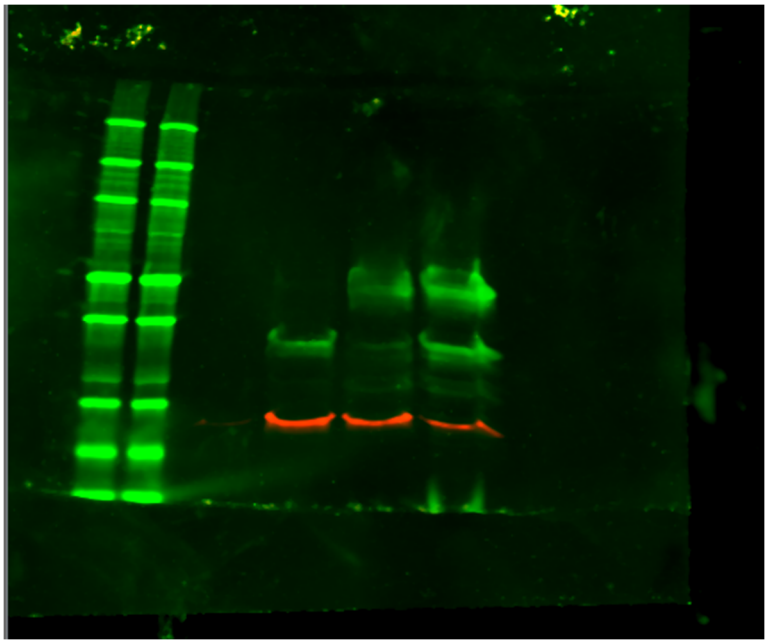

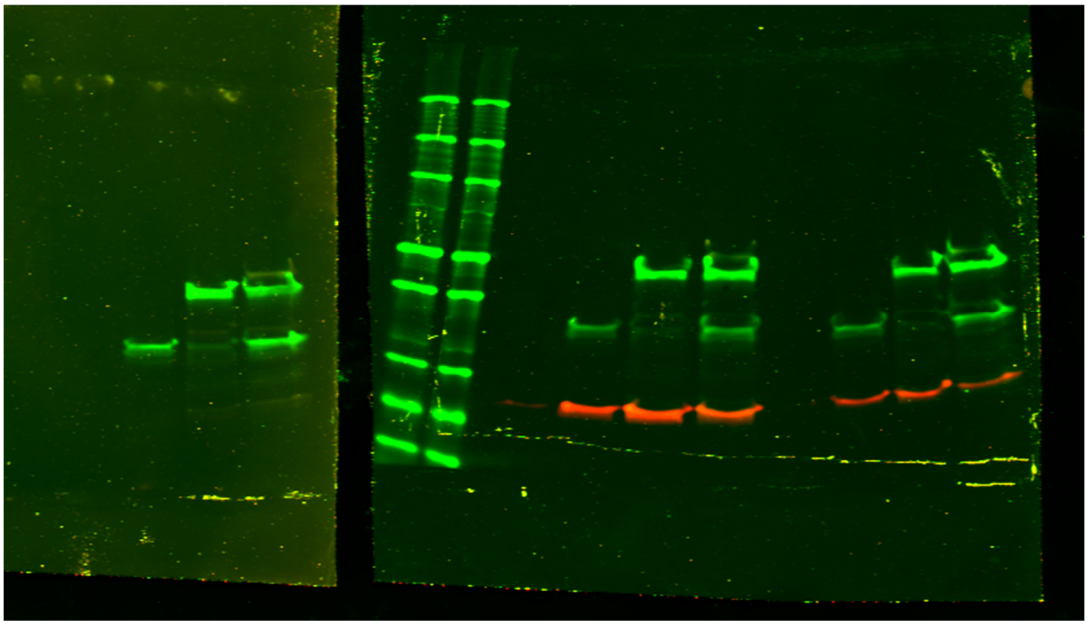

Supplementary Figure 5 – panel F (autoradiograms)

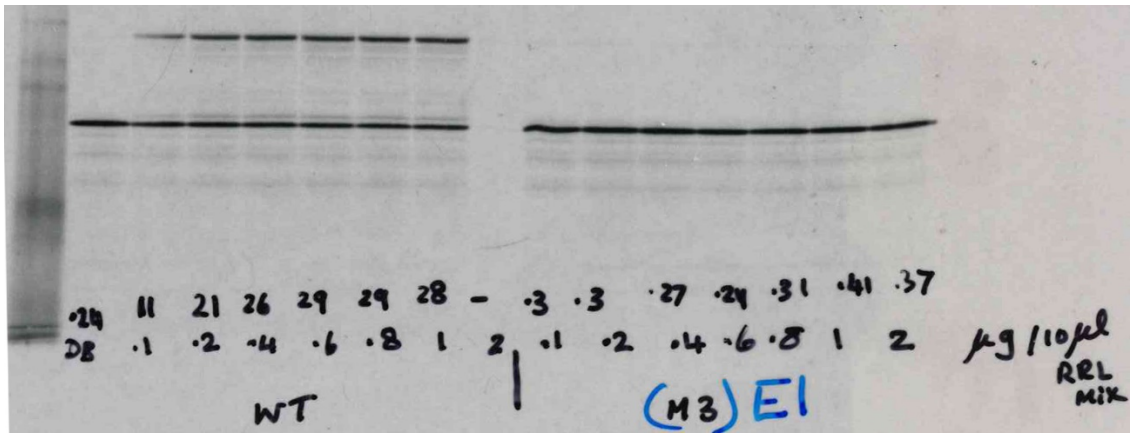

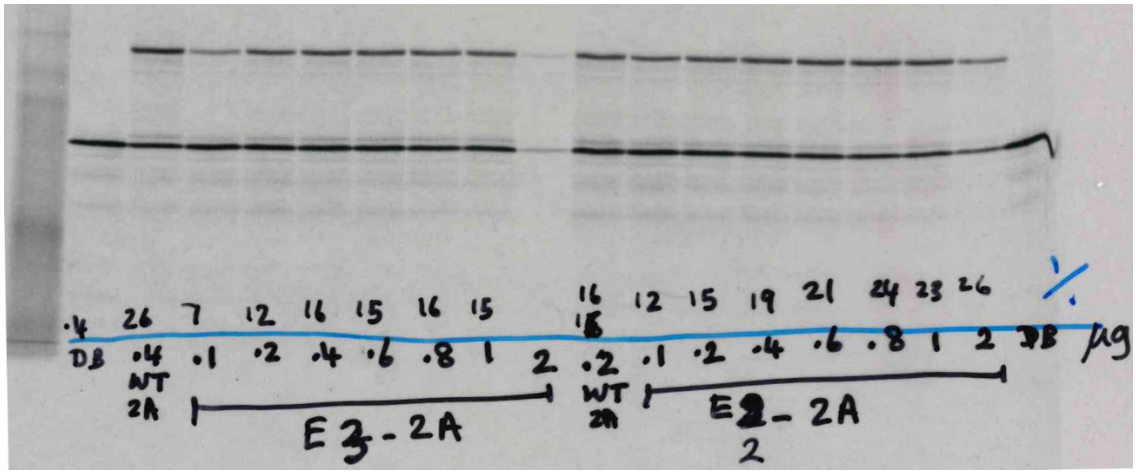

Supplementary References

1. Svitkin, Y.V., Hahn, H., Gingras, A.C., Palmenberg, A.C. & Sonenberg, N. Rapamycin and wortmannin enhance replication of a defective encephalomyocarditis virus. *J Virol* **72**, 5811-9 (1998).
2. Petty, R.V., Basta, H.A., Bacot-Davis, V.R., Brown, B.A. & Palmenberg, A.C. Binding interactions between the encephalomyocarditis virus leader and protein 2A. *J Virol* **88**, 13503-9 (2014).
3. Groppo, R., Brown, B.A. & Palmenberg, A.C. Mutational analysis of the EMCV 2A protein identifies a nuclear localization signal and an eIF4E binding site. *Virology* **410**, 257-67 (2011).
4. Lin, J., Gagnon, M.G., Bulkley, D. & Steitz, T.A. Conformational changes of elongation factor G on the ribosome during tRNA translocation. *Cell* **160**, 219-27 (2015).